THIRTEEN

Remote sensing of impact craters

Shawn P. Wright[*], Livio L. Tornabene[†] and Michael S. Ramsey[‡]

[*]*Institute of Meteoritics, MSC03 2050, University of New Mexico, Albuquerque, NM 87131, USA*
[†]*Centre for Planetary Science and Exploration, Department of Earth Sciences Western University, 1151 Richmond Street, London, ON, N6A 5B7, Canada*
[‡]*Department of Geology and Planetary Science, University of Pittsburgh, 4107 O'Hara Street, Pittsburgh, PA 15260-3332, USA*

13.1 Introduction

As discussed throughout this book, impact cratering is a fundamental geological process that has shaped and modified the surfaces of planets throughout geological time (see summary in Chapter 1). However, the low frequency of meteorite impacts during the recent past and the ongoing active geological processes on Earth offer rare opportunities to examine pristine impact sites, which are common on the surfaces of other terrestrial planets. With the exception of a few robotic and manned space exploration missions, the analysis of orbital data has been the primary method for studying impact craters in a variety of settings and target rocks throughout the Solar System. In this chapter, an overview of remote-sensing datasets and techniques is presented with direct applications to the study of impact craters. Various types of data, as well as methods and techniques for processing and interpreting these datasets, are summarized. For readers who are interested in a more in-depth discussion of the datasets and techniques mentioned in this chapter, refer to Vincent (1997), Sabins (1997), Lillesand and Kiefer (2000) and Jensen (2007), and refer to Garvin *et al.* (1992), French (1998) and Koeberl (2004) for overviews of remote sensing specifically applied to impact crater studies.

The goal of remote sensing is to provide useful information about planetary surfaces prior to fieldwork, sample collection or *in lieu* of such work in the cases where access may be limited or not possible. The basic principle involves collecting, understanding and using data acquired as a result of the interaction between matter (i.e. rock or surface) and electromagnetic energy (e.g. infrared wavelengths). A variety of remote-sensing datasets and techniques have been used to determine: (1) geology; (2) morphometry/altimetry/topography; (3) composition; and (4) physical properties (e.g. particle/block size, thermal inertia). Different wavelength regions as well as derived datasets and data processing techniques can be utilized to determine one or more of the aforementioned surface properties with applications to the study of impact cratering. This chapter addresses these four themes, followed by two case studies that utilize one or more of these aspects to solve a geological problem about an impact site.

13.2 Background

An early and ongoing goal involving remote sensing of terrestrial impact craters has been to simply discover new impact craters solely from remote-sensing data (Garvin *et al.*, 1992; Koeberl, 2004; Folco *et al.*, 2010, 2011) or find spectral differences between shocked rocks and their protoliths (D'Aria and Garvin, 1988; Garvin *et al.*, 1992; Johnson *et al.*, 2002, 2007; Wright *et al.*, 2011). Photogeology, or image analysis, is used to search for the distinctive circular structure of an impact crater, in addition to terraces and central peaks within larger complex craters (see Chapter 5). Several impact structures have been found with this method (e.g. Folco *et al.*, 2010, 2011). Remote sensing alone, however, cannot provide definitive evidence for impact, as many circular structures can be formed by other geological processes (e.g. sinkholes, granite or salt domes, volcanoes). Impact structures can be identified by the recognition of a suite of characteristic impactites (see Chapter 7) and shock metamorphic effects (see Chapter 8); however, this is difficult (albeit not impossible) to accomplish via remote sensing and/or spectroscopy. Impactites, as discussed in Chapters 7 and 9, consist of a variety of impact breccias and melt rocks generally with the same composition as the original target rocks. In some cases, impactites exhibit geochemical enrichments (Chapter 15) from the impactor and/or mineralogical changes due to shock that are difficult to measure from spaceborne instrumentation. Images with very high spatial resolution are commonly required to resolve impact breccias, which must have exposed clasts larger than the spatial resolution of the imaging instrument. The current highest pixel dimensions of modern imaging systems is on the order of tens of centimetres, and thus megabreccias are most easily identified (e.g. Grant *et al.*, 2008; Marzo *et al.*, 2010; Fig. 13.1). Breccias with smaller exposed clasts will be difficult to identify.
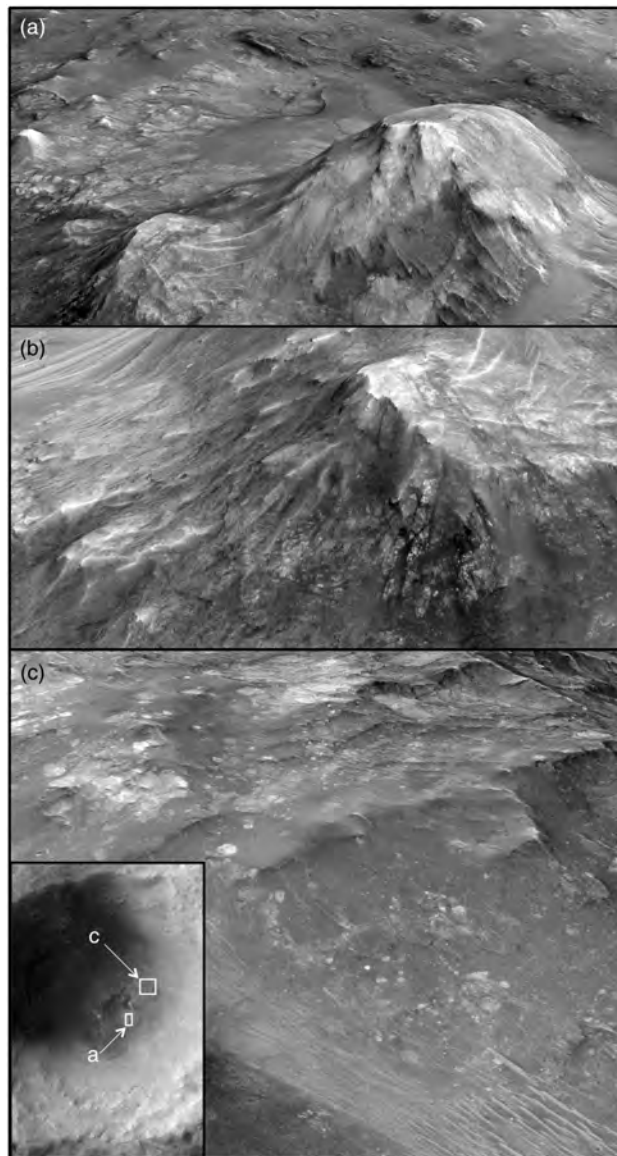
Figure 13.1   Various portions of a HiRISE red mosaic image (PSP_005842_1970) covering the eastern portion of the central uplift complex of the approximately 40 km Toro crater, Mars, are shown to demonstrate the use of topographic data. The image is draped on a digital terrain model (DTM) derived using SOCET set v5.4.1 (BAE systems) and the PSP_005842_1970 and ESP_011538_1970 stereo pair (credit: NASA/JPL/UA); resolution is 2 m/pixel with a vertical exaggeration of approximately 5×). (a) A portion of the HiRISE red mosaic image (PSP_005842_1970; ~1 km across from the base to the summit of the uplifted and rotated megablock) covering the southeastern portion of Toro's central uplift complex and crater floor. The perspective view is slightly to the northeast. The uplifted megablock, although covered with fine-grained debris and talus, shows evidence of the underlying light-toned, fractured and brecciated bedrock. A smaller megablock on the lower left shows what appear to be breccia dikes consistent with field observations of central uplift bedrock within terrestrial impact structures. (b) A rotated and close-up view of the smaller megablock exhibiting the dike-like structures in (a). These could be pseudotachylites or possible impact melt-bearing breccia dikes that were injected into the crater floor during the formation and expansion of the transient cavity, and subsequent formation of the central uplift. (c) A perspective view to the south-southwest of Toro's crater-fill deposits. These deposits are observed to drape the uplifted bedrock of the central uplift complex and are continuous with the crater-fill deposits on the crater floor. These materials are relatively smooth, dark toned and possess abundant light-toned megaclasts. The unit is interpreted to be an impact melt-bearing breccia deposit formed by materials that once lined the transient cavity of Toro during the excavation phase of crater formation. Reprinted from Marzo *et al.*, 2010, with permission from Elsevier.

13.3 Photogeology

Photogeology is the use of aerial or orbital data to view and interpret geological and geomorphologic features. Geologists have used aerial photographs for decades to: (1) determine rock exposures from surfaces with and without vegetation; (2) study the expression of landforms for insight into their origins (geomorphology); (3) determine the structural arrangements of disturbed bedrock (i.e. folds and faults); (4) evaluate dynamic changes from natural events (e.g. floods; volcanic eruptions); and (5) use as a visual base map, commonly in conjunction with topographic maps, on which a more detailed map can be derived (e.g. a geological map).

The advantage of a large, synoptic view of a study region allows for the examination of structures or features of interest in their entirety, whereas a field geologist likely could not map a large area in a short time. The ability to merge different types of remote-sensing data discussed in this chapter can further facilitate the recognition of relationships between various surface components to be determined with specific applications towards impact cratering studies. Figure 13.2 illustrate the types of images used for photogeologic analyses of three craters and describe various spatial resolutions and examples of using false-colour images and more than one type of remote-sensing analysis of an impact site.

13.4 Morphometry, altimetry, topography

Elevation can be extracted using photometric stereo data processing, as well as from active techniques such as radar and laser altimetry. The latter can produce high-resolution DTMs that provide three-dimensional (3D) geospatial visualization and characterization of impact-related features. Elevation data can also be combined with other datasets to create 3D visualizations that facilitate correlations with spectral units and/or high-resolution morphologic units, and also for interpretation of structural/stratigraphic relationships. The terms 'laser altimetry' or formerly 'laser-induced swath mapping' has been replaced by the acronym LiDAR (light detection and ranging). Depending on the instrument, either ultraviolet, visible or near-infrared energy is backscattered or reflected from the surface and the distance from the instrument to the ground is calculated by measuring the time delay between the transmission of the laser pulse and the detection of the reflected signal. This creates high-resolution topographic data from millions of data points from a scanning swath width instrument to dozens of gridded points from an orbital system where the laser pulse is backscattered every several metres.

One of the primary uses of topographic data, particularly with respect to planetary applications for impact craters, is the measure of morphometric aspects of these features, such as depth, diameter, volume of crater-fill and various aspects of crater ejecta (e.g. Stewart and Valiant, 2006). In most cases, visible laser altimeters have been employed to derive gridded global DTMs of planetary surfaces (Zuber *et al.*, 1992; Smith *et al.*, 2001, 2010). Furthermore, for craters on Earth, these data can be used by field geologists to correlate features mapped on the ground (e.g. Zumsprekel and Bischoff, 2005). Another method for deriving morphometry and altimetry is the use of individual or paired stereo images (i.e. obtained from at least two viewing angles and having a proper separation to reproduce the third dimension). These stereo images are typically processed into a standard qualitative image anaglyph (red–blue images showing relative elevation) or into a more quantitative DTM (e.g. Fig. 13.1, Fig. 13.3 and Fig. 13.4). For the 3D analysis of terrestrial craters, numerous options exist that include datasets such as the Shuttle Radar Topography Mission (SRTM; e.g. van Zyl, 2001; Farr *et al.*, 2007) and the global digital elevation model (GDEM) product created by the stereo imaging capability of the Advanced Spaceborne Thermal Emission and Reflection Radiometer (ASTER) sensor (e.g. ASTER, 2010) to high-resolution airborne LiDAR flown over specific targets. The global datasets have DEM resolutions on the order of 30 m/pixel, whereas airborne LiDAR can have very high resolutions (on the order of centimetres).

Scanning LiDAR is a powerful tool that can also acquire data of the surface topography (Bufton *et al.*, 1991) independent of local vegetation and other ground cover. With enough data points, a statistically significant number of laser pulses will miss vegetation cover and reflect off the ground surface rather than (tall) vegetation. The laser pulses that reflect off vegetation can then be statistically filtered to create a 'bald earth' model, which can be used to trace faults and other subtle surface features (Webster *et al.*, 2006; Prentice *et al.*, 2009). As an example of its high accuracy, LiDAR has also been used for change detection (Woolard and Colby, 2002). This can be especially useful for assessing the structure and morphology of terrestrial impact structures covered by dense vegetation (after filtering). The example shown (Fig. 13.5) is not from an impact crater, but displays the utility of using LiDAR.
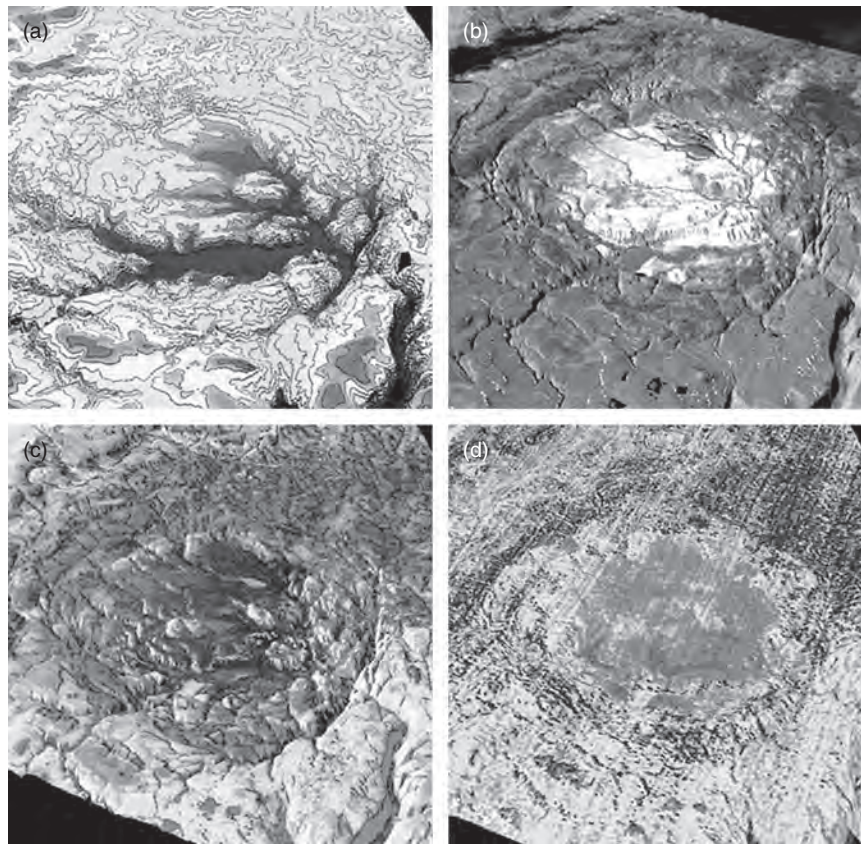
13.5 Composition derived from remote sensing

Measurements of the electromagnetic spectrum are only practical within certain wavelength regions, as they provide specific diagnostic information ranging from atomic/molecular interactions to physical properties of surface materials. Some wavelength regions useful for diagnostic compositional analysis of the surface using remotely sensed data may be obscured by absorption or scatter in the atmosphere of the planetary body being observed. In order to quantitatively extract the position, shape and magnitude of surface spectral features, one must take into account: (1) the interaction of that energy with materials on the surface; (2) the passage of that energy through the intervening atmosphere; and (3) the subsequent capture of that energy and response by the instrument detectors. All of these interactions need to be understood and well constrained in order to extract and separate the atmospheric and surface spectra. Absorption and scattering by water vapour, carbon dioxide and stratospheric ozone in the Earth's atmosphere, for example, cause all of the gamma-ray region, most of the ultraviolet and thermal infrared (TIR) region, and some of the visible to near-infrared (VNIR) and shortwave infrared (SWIR) regions to be obscured (Hudson, 1969). This is
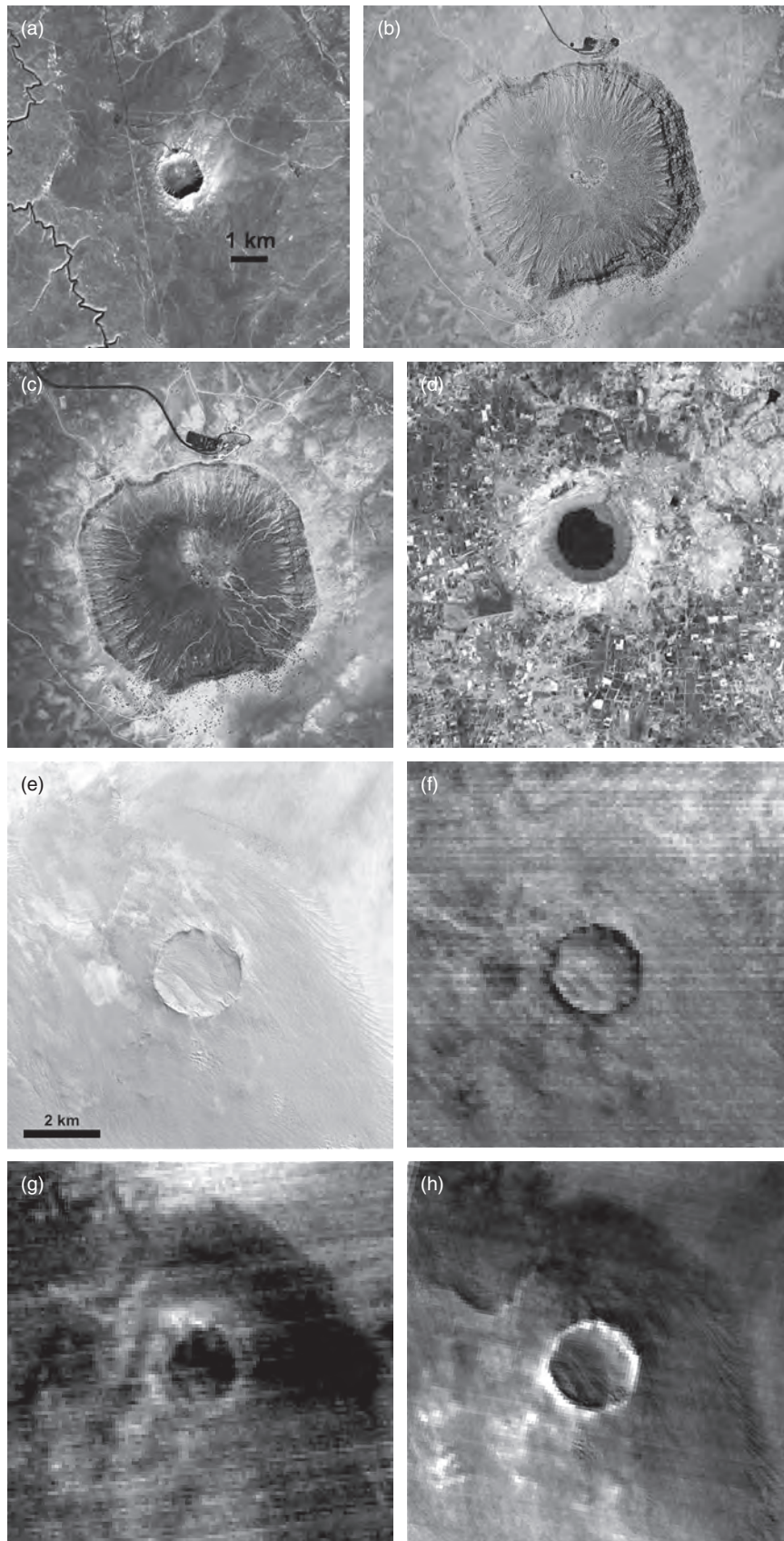
Figure 13.2 (a) 15 m resolution ASTER VNIR of Meteor Crater, Arizona displayed as bands 3–2–1 in red–green–blue (refer to Colour Plate 29), showing very little vegetation save for a small farm with trees east of the crater. (b) True-colour aerial photograph of Meteor Crater with approximately 1 m resolution. (c) False-colour aerial photograph of Meteor Crater stretched to display ejecta lobes of bright-white Coconino and Kaibab ejecta. (d) False-colour ASTER VNIR image of Lonar Crater, India (Chapter 18), displayed as bands 3–2–1 in red–green–blue; vegetation (as red) can be seen circum the crater lake but inside the crater rim. (e)–(h) ASTER VNIR and TIR data of Roter Kamm, Namibia; (e) daytime VNIR colour image showing the pervasive mantling of aeolian sand; (f) daytime TIR decorrelation stretch of TIR bands 14, 12, 10 in R, G, B (respectively) indicating significant variability in the sand composition (Fe-rich silicate sands shown in blue/purple and non-Fe-rich silicates shown in red); (g) night-time temperature image showing less than 4 °C variation from crater rim to the near-rim ejecta; (h) apparent thermal inertia (ATI) image (see text) with high ATI values (bright) indicating potential blocky and less mantled ejecta. See text for explanations of acronyms. (See Colour Plate 29)
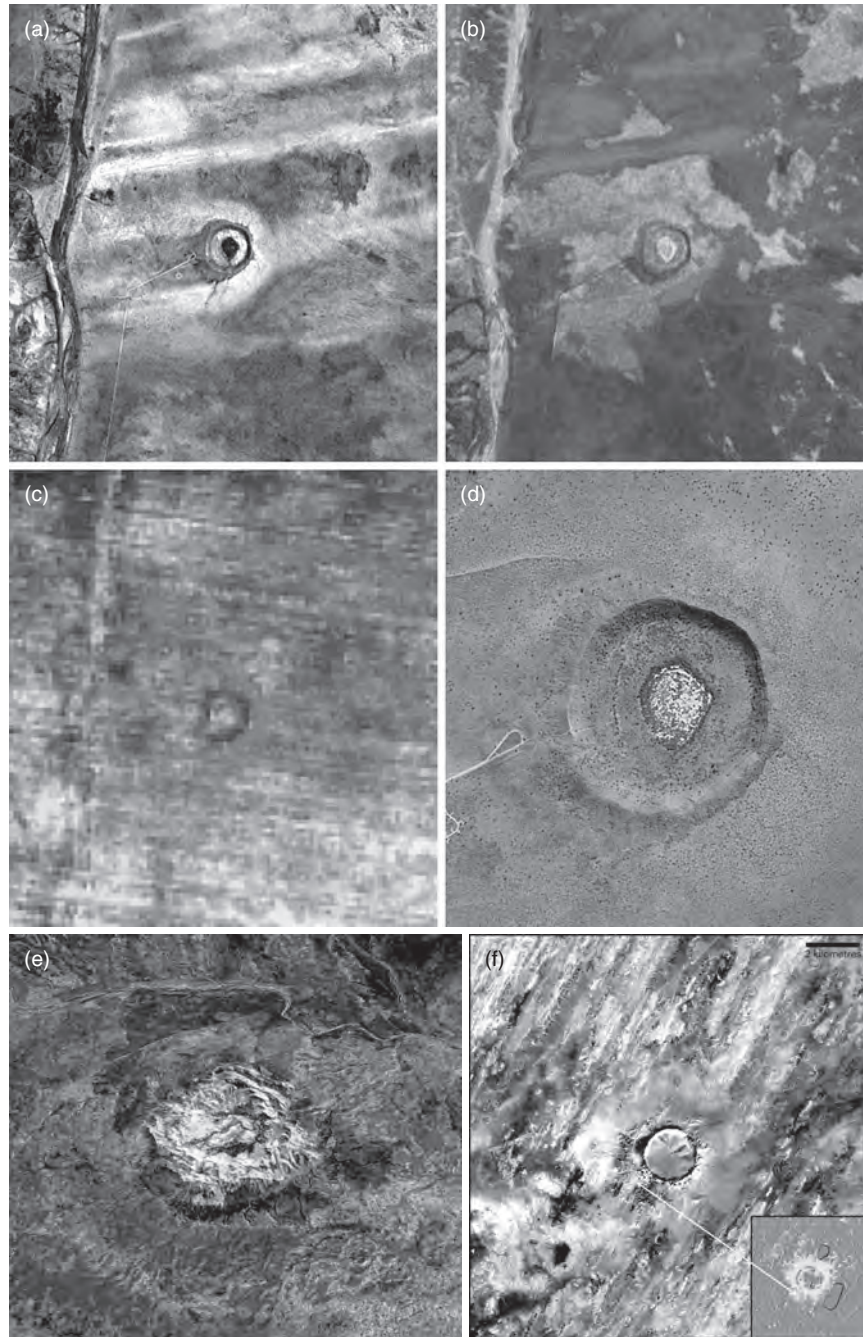
Figure 13.3 Various remote images of the Wolfe Creek (a–d) and Gosses Bluff (e) craters in Australia. (a) ASTER VNIR image with bands 3, 2 and 1 displayed as red, green and blue (see Colour Plate 30), with a 2% stretch. Image taken 02-02-2003. (b) Landsat band ratio image with Fe ratio, normalized difference vegetation index and OH-bearing ratio (see text for details) displayed as red, green and blue. Data are stretched 2% to bring out differences. Image from 09-03-1999. (c) ASTER TIR decorrelation stretch with bands 14, 12 and 10 displayed as red, green and blue. Image from 02-02-2003. (d) High-resolution image derived from © Google Earth, 2012. (e) View to northwest of the 23 km diameter Gosses Bluff Crater, with a hue saturation value transformed VNIR with SWIR minimum noise fraction (MNF) bands applied to a VNIR image (15 m resolution) and draped on a DTM with a vertical exaggeration of 3. Green represents bedrock from several Mesozoic sandstone lithologies (Barlow, 1979; Prinz, 1996) uplifted above alluvium shown as blue and purple. (f) ASTER stereo-derived DEM and VNIR data covering the 1.9 km terrestrial impact structure Tenoumer located at 22°55′7″N, 10°24′29″W, in Mauritania, Africa. The 15 m/pixel colour infrared image of Tenoumer reveals what appears to be a two-facies, circumferential deposit around the crater rim reminiscent of ejecta around fresh impact craters on other planetary surfaces. The colour-coded DEM in the inset shows elevated terrain consistent with the inner most facies of these deposits, which strongly supports the idea that some ejecta was preserved around this infilled simple crater. The DEM shows similar to results from Meteor Crater (Garvin *et al.*, 1989), that the wind regime that has dominated this region since the time of crater formation has preferentially muted and eroded the windward (southwest) side. (Note: the two areas outlined in black and in solid purple are areas of spurious data values where difficulties due to surface or atmospheric properties confounded attempts to derive digital elevation for these areas.)

Figure 13.4 Morphometric and spectral maps (VNIR, SWIR and TIR) of the Haughton impact structure, Devon Island, Nunavut territory, Canada. North is to the bottom right of each subimage. (a) A 25 m colourized DTM of the Haughton impact structure (courtesy of the Natural Resources of Canada http://www.nrcan-rncan.gc.ca/com/index-eng.php), with the vertical exaggeration set to 10. (b) VNIR image from *Landsat 7* ETM+ (30 m/pixel). The impact melt rock of the Haughton Formation is the most apparent lithological unit. This is manifested as a white unit that predominately lines the crater floor, but smaller occurrences can also be observed in the vicinity of the wall/terraces and rim area. (c) ASTER SWIR (1.656–2.400 μm) colour composite of MNF-transformed bands using principle components 2, 1 and 6 in RGB (30 m/pixel). Lithological units are as follows: magenta, dolomite; cyan, limestone; red, gypsum; blue, impact melt rock. (d) ASTER TIR colour-composite using DCS bands 14, 12 and 10 (90 m/pixel; Tornabene *et al.*, 2005). Lithological units are as follows: dark blue–green is dolomite; cyan–light green is limestone; red is gypsum; and magenta–pink is impact melt rock. (See Colour Plate 31)

less of an issue for the microwave portion; however, even within a relatively clear atmospheric window, scattering/emission can still occur, which can further complicate an accurate analysis of the surface spectra for specific mineral features. Because the various wavelength regions can provide information as varied as elemental, mineralogical and thermal details of the surface, each is summarized below by wavelength region.

13.5.1 Gamma and ultraviolet

As all gamma rays and virtually all ultraviolet light is absorbed by the Earth's ozone layer, these data are not typically analysed for terrestrial applications and, hence, are not discussed in detail here. On other planets lacking atmospheric ozone (or atmospheres for that matter), such as the Moon and Mars, gamma ray and neutron remote sensing can be used to place constraints on the elemental composition of the uppermost approximately 1 m of the surface, including the presence of hydrogen inferred to be subsurface water ice. However, very large pixel sizes common in this wavelength region generally prevent detailed analyses of all but the largest impact craters and basins. For example, the Mars Odyssey Gamma Ray Spectrometer has a spatial resolution of approximately 300 km per pixel (Boynton *et al.*, 2004).

13.5.2 Visible to near-infrared (VNIR) to shortwave infrared (SWIR)

The most familiar type of remote sensing involves detecting energy in the 0.4–0.67 μm wavelength region. This includes aerial and satellite-based images of Earth and other planets (Fig. 13.2 and Fig. 13.3a). In general, this wavelength region is the most easily understood, and has had the longest period of technological
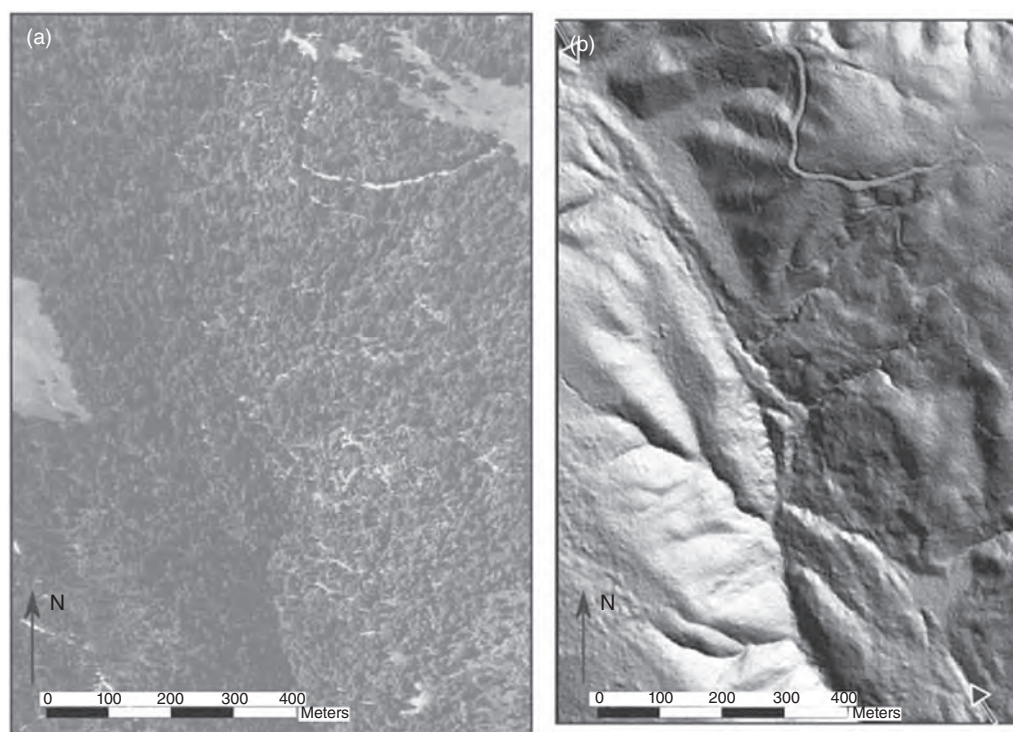
Figure 13.5   Analysis of the San Andreas fault from Prentice *et al.* (2009). (a) Aerial photograph of the fault obscured by a dense vegetation canopy. (b) Hillshade image of same area shown in (a) derived from LiDAR after removal of the vertical vegetation structure. The San Andreas fault (arrow) and several minor topographic features can be seen in much more detail. Similar data of terrestrial impact sites may permit the identification of previously unmapped faults and fractures.

development through extensive use by the military, commercial and scientific communities. Compositional properties, in addition to morphology, morphometry and altimetry (via stereo observations), can be gleaned using visible data. The VNIR 0.4–2.6 µm wavelength region is particularly sensitive to changes in valence and the energy state of the outer electrons of transition metals (e.g. Fe^{3+} or Fe^{2+}) and vibrations between atoms chemically bonded in mineral structures (e.g. OH^- and H_2O). The electrons and vibrating molecules absorb or reflect radiation at characteristic frequencies, leading to distinctive spectral features that are diagnostic of characteristic metal cation–anion bonds. Generally, electronic transition absorptions are broad and occur at wavelengths shorter than approximately 1.5 µm, whereas sensitivity to bond vibrational energy generally occurs at wavelengths longer than this. Depending upon band positions, multispectral data (generally <10 bands) can be used to distinguish several mineral groups, but hyperspectral data (tens to hundreds of bands) is commonly required in order to accurately identify specific minerals based on their image-derived spectra. These spectra can be compared with a spectral library of laboratory-measured rocks and minerals. Most clays, sulfates and iron-bearing minerals, such as pyroxene and olivine, all have diagnostic VNIR absorptions, whereas unhydrated silica phases, chlorides, glasses and some sulfates and oxides do not, and thereby are difficult if not impossible to detect using this particular wavelength range.

13.5.3   Thermal infrared (TIR), including mid-infrared to far infrared

Vibrational spectroscopy (also known as mid infrared (MIR) and TIR) involves the measurement of emitted energy of planetary surfaces over approximately the 3–50 µm region and has been used as a tool to address a variety of geological problems requiring major rock-forming mineral identification and mapping. This is made possible because many of these materials display prominent spectral absorption features (emissivity lows/reflectance highs) within this wavelength region. In the context of geological studies, spectral features arise from the bending/stretching frequencies of the Al–Si–O and Ca–O bonds, for example, making TIR remote sensing excellent for the study of silicate and carbonate rocks on planetary surfaces (Lyon, 1965; Hunt, 1980; Salisbury and Walter, 1989). In order to compare emitted spectra of planetary surfaces with those from the laboratory, the surface radiance must be separated into the temperature and emissivity components to facilitate comparisons between them. The emitted radiance is described by the Planck equation, which states that perfectly emitting surfaces (i.e. blackbodies) do not have temperature–wavelength-dependent variations (Realmuto, 1990; Gillespie *et al.*, 1998). Fortunately, most natural materials and surfaces are not blackbodies and have spectral features at characteristic wavelengths as a result of the asymmetric bonds of the minerals they contain (Salisbury and D'Aria, 1992; Salisbury and Wald, 1992; Salisbury, 1993).

For the TIR emissivity of most rocks and soils, the photon–matter interaction of the component minerals can be modelled as linear combinations because of the high absorption coefficients (Gillespie, 1992; Adams *et al.*, 1993; Ramsey and Christensen, 1998). This property results in simple surface (Fresnel) reflections of the emitted photons. These photons have a much shorter path length relative to the particle size and, therefore, generally interact only once after being emitted/reflected from particles. These photons either reach the detector containing only information about that particular particle, or they are quickly absorbed after being scattered and never reach the detector. As a result, the majority of the energy detected remotely has interacted with only one surface particle and the spectral features from the surface particles are retained in proportion to their areal extent.

Mixing of emitted energy from spectral end-members occurs at all scales. What defines a component or end-member depends on the scientific goals of the study (e.g. specific minerals, rock units, sand populations, micrometre-scale surface textures). For cases such as these, a more complex data extraction model is required in order to positively identify the presence and amount of a particular end-member within a TIR scene. If the pure mineral spectra (end-members) are known in advance, this allows TIR spectra to be linearly deconvolved (i.e. unmixed) in order to ascertain the areal percentages of end-member constituents (i.e. mineral or rock components) within the field of view of the instruments and several micrometres into the surface (Thomson and Salisbury, 1993; Ramsey and Christensen, 1998; Ramsey and Fink, 1999; Hamilton, 2003; Wright and Ramsey, 2006; Carter *et al.*, 2009). However, non-isothermal surfaces or very fine grained surface materials (grains with sizes smaller than or on the order of the wavelength) behave non-linearly with respect to their components (Gillespie, 1992; Ramsey and Christensen, 1998).

13.6 Physical properties derived from remote sensing

13.6.1 Thermophysical properties

In addition to the spectral information derived from TIR data, the radiant energy also contains temperature information that can be used to determine information deeper than the uppermost surface layer (i.e. thermophysical properties). Thermophysical properties include brightness temperature, thermal inertia and estimates of rock abundance (as described in Fergason *et al.* (2006) and Nowicki and Christensen (2007)). Thermal inertia is a measure of the resistance of a material to change in temperature and can be calculated accurately if a material's thermal conductivity, density and specific heat are known. Unfortunately, these variables cannot be obtained directly from remote sensing, and thus a thermal model of the surface is needed that relies on several assumptions in conjunction with infrared radiance data to derive both temperature and thermal inertia (Cracknell and Xue, 1996; Fergason *et al.*, 2006). For the Earth, the Moon and Mars, thermal inertia is an excellent proxy for particle size of surface materials, and is used to discriminate bedrock and various grain-sized unconsolidated deposits (coarse sands down to 'dust'-sized

particles). Similarly, both brightness temperature and thermal inertia have been used for a more accurate understanding of impact sites on Mars (e.g. Pelkey *et al.*, 2001; Christensen *et al.*, 2003; Tornabene *et al.*, 2005; Wright and Ramsey, 2006), and more recently for the Moon (Bandfield *et al.*, 2011). Changes in the particle size and/or thermophysical properties can also help to derive soil moisture, detect crater rims buried by thick sand deposits and distinguish ejecta from the surrounding terrain, as shown with high-resolution TIR data of Mars (Christensen *et al.*, 2003; Wright and Ramsey, 2006) and Roter Kamm Crater in Namibia (Fig. 13.2h). Cracknell and Xue (1996) reviewed how to calculate thermal inertia values from remote-sensing data.

13.6.2 Surface roughness from microwave imaging (i.e. radar)

The basic principle of radar (former acronym for 'radio detection and ranging') remote sensing involves the acquisition and processing of microwaves that have interacted with materials (~1 cm to several metres in wavelength). In side-looking radar, radar pulses are transmitted at an angle (the depression angle) by the airborne or spaceborne instrument after which the energy, timing and polarization of the reflected energy are captured. Surface roughness, on the scale of the incident wavelength, is the primary attribute measured. 'Rough' and coarse-grained surfaces (centimetres to metres) generally reflect the radar wave back to the detector, whereas low-return surfaces with fewer reflections are interpreted as 'smoother' or fine grained. A surface with higher dielectric constants (i.e. soil moisture, metals and buried ground ice) will also increase the radar return.

The best example of radar remote sensing used for analysis of craters on planetary surfaces is the global mosaic of Venus collected by the *Magellan* spacecraft. The surface of Venus is obscured to most remote-sensing techniques by a thick, CO_2-rich, approximately 90 bar atmosphere; however, radar waves can penetrate thick planetary atmospheres (e.g. Venus and Titan). Therefore, radar is commonly the remote-sensing dataset chosen to examine such bodies, although some infrared datasets are also useful (e.g. Brown *et al.*, 2004). After the *Pioneer Venus Orbiter* spacecraft's radar altimeter allowed for the earliest topography of Venus, albeit with a 150 km surface resolution (Masursky *et al.*, 1980; Pettengill *et al.*, 1980), *Magellan's* 12.6 cm radar wavelength data gave better views of the impact craters on the Venusian surface (Saunders *et al.*, 1990). It also revealed a surprising paucity of craters on Venus, indicating a younger surface than previously suspected. The *Cassini* spacecraft's Titan Radar Mapper (1.88 cm wavelength) acquired radar images of Titan that showed craters. Figure 13.6 highlights examples of complex craters with bright and dark interior and exterior deposits imaged on Venus and Titan. Radar-bright areas are generally coarse grained or 'rougher' than radar-dark areas. Hummocky crater-fill deposits and ejecta blankets are commonly radar bright, whereas radar-dark surfaces are finer grained or 'smoother'. The radar images of complex craters in Fig. 13.6 exhibit several attributes of fresh complex craters: ejecta, rim, wall/terraces and a central peak. Several workers have focused on radar data of impact sites on Venus and Titan (Phillips *et al.*, 1991; Schaber *et al.*, 1992; Campbell
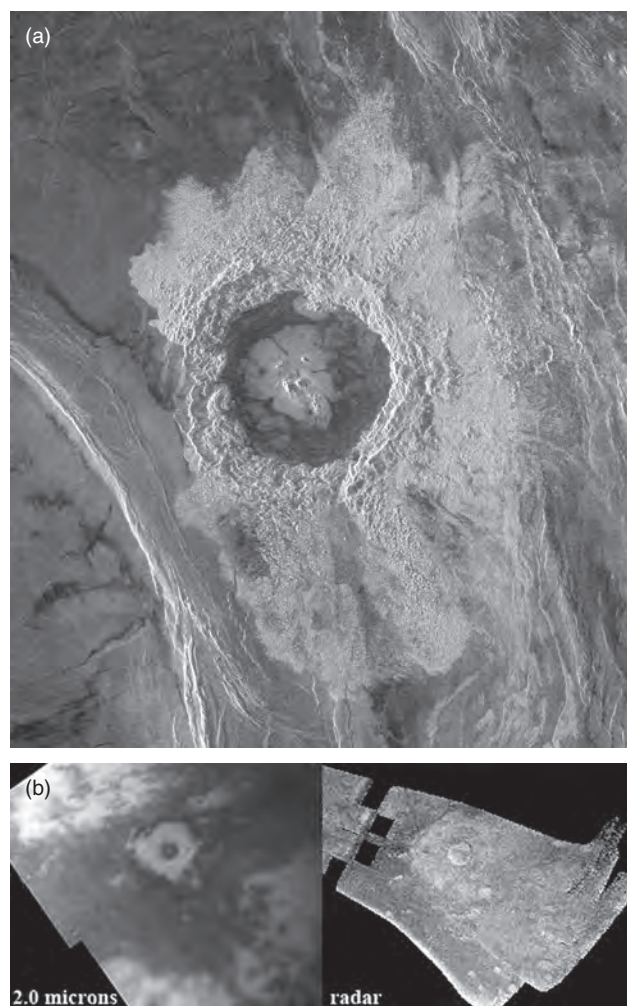
Figure 13.6 (a) *Magellan* radar image (12.6 cm wavelength) of Dickinson Crater on Venus, an approximately 69 km diameter complex crater exhibiting a radar-bright crater rim and wall/terrace region, and both 'smooth' and 'rough' interior deposits. The ejecta deposits are both very bright (rough) in the northern ejecta and show some less bright to darker portions (smoother) in the southern ejecta, whereas the crater interior shows a 'rough' central peak surrounded by a smoother crater floor. (Image credit: NASA/JPL; Image PIA00479: http://photojournal.jpl.nasa.gov/.) (b) *Cassini* orbiter images of one of Titan's few impact craters imaged in near infrared (left) and radar (right). The impact crater is an approximately 80 km diameter complex crater (note the 'darker' central peak feature at 2.0 μm and its outline in radar). (Image credit: http://photojournal.jpl.nasa.gov/catalog/PIA07868.)

et al., 1992; Chadwick and Schaber, 1993; Lorenz *et al.*, 2007; Le Mouélic *et al.*, 2008; Wood *et al.*, 2010). Recent work has showed the utility of using a particular type of radar called circular polarization ratio radar to identify secondary craters on the Moon (Wells *et al.*, 2010).

13.7   General spectral enhancement and mapping techniques

Various methods of enhancing spectral features on remote images are briefly described here. For more information, consult chapters concerning this topic in textbooks (Vincent, 1997; Sabins, 1997; Lillesand and Kiefer, 2000; Jensen, 2007). With an understanding of the properties discussed above, it is the scientist's task to visually display a feature or characteristic of the crater or geological scene under study using remote data. Several of the more common approaches are described here, with further detail on certain methods provided in the case studies in Section 13.8.

With multispectral data, there are limited colour combinations one can make to emphasize mineral and lithological spectral variability in a scene. Individual inspection of bands is typically necessary in order to determine which areas are affected by absorptions at a particular wavelength. By noting which bands show the most variability, one can simply make a first-order spectral map by placing three of these bands into red, green and blue (R–G–B). Spectral units are contiguous areas of similar spectral properties (i.e. colour) contained in the scene. Related to this approach is creating band ratios (e.g. dividing a wavelength channel positioned on the continuum of a spectrum by a channel positioned within the deepest portion of an absorption feature) for the purpose of mapping the presence of diagnostic absorption features. Band ratioing is most useful for multispectral imagery that lacks the spectral resolution needed for direct matching to specific library spectra (e.g. ETM+ or ASTER data for Earth or Thermal Emission Imaging System (THEMIS) data for Mars), and has been used extensively to map specific mineral groups in terrestrial remote-sensing studies (e.g. Rowan and Mars, 2003; Fig. 13.3b). In the event that colour differences are subtle where the band-to-band data are highly correlated, a decorrelation stretch (DCS) can be applied (Fig. 13.2f, Fig. 13.3c and Fig. 13.4d). The DCS identifies the major axes of correlation, stretches data perpendicular to these axes and, thus, fills the entire dynamic range of the colour space while retaining the original hues of the units in the original R–G–B composite (Gillespie *et al.*, 1986). Additional mapping techniques include the MNF transform noise (Boardman and Kruse, 1994), a type of principal component (PC) analysis, which is designed to decrease the dimensionality of hyperspectral datasets (Fig. 13.4c). Such techniques are necessary for large (hyperspectral) datasets where it would not be practical to inspect all bands individually. These techniques reduce the spectral variability in a data cube containing hundreds of bands to as few as a dozen bands with each one being individually influenced by an important surface attribute, such as albedo, illumination, temperature and individual spectral components (i.e. compositional variability). Another means of analysing hyperspectral variability is to identify the image-derived spectral endmembers (IEMs) in a scene, which typically represent the purest spectral components that can be resolved within the spatial and spectral limits of the dataset (i.e. purest mineral and lithological compositions). The significance of such a classification is that, ideally, every pixel within a scene can be potentially described as a mixture of these purest end-member spectra, and the distribution and concentration of each IEM can be displayed. Generally,

displaying the abundance of each IEM is more easily understood than displaying individual bands or values.

13.8 Case studies

Two examples are described below that demonstrate the usefulness of remote sensing in determining the distribution of lithologies at impact craters. The composition of the Haughton impact structure (HIS), Canada, and Meteor Crater, Arizona, USA, are related to the pre-impact stratigraphy and erosion since impact.

13.8.1 VNIR, TIR and DEM analyses of the HIS, Canadian Arctic

In lieu of, or in addition to, *a priori* knowledge from the field, remote-sensing techniques can be used to construct lithological maps of terrestrial impact structures that are well exposed and well preserved in areas with low vegetation coverage. Such maps are reasonably accurate with respect to features on the order of about three or four pixels and can be used prior to mapping and sampling in the field, or generally augment observations from the field. As a specific example, we present a summary of the work of Tornabene *et al.* (2005) on the lithological mapping, via spectral analyses of multiple spaceborne datasets, of the HIS – an approximately 23 km diameter complex crater centred at 75°22′N, 89°41′W on the western part of Devon Island, in the Canadian Arctic Archipelago, Nunavut. The HIS is particularly well suited for study by remote-sensing spectral and mapping techniques as: (1) the structure is sizable enough for lithological units to be resolved spectrally using the spatial resolution of the available orbital datasets; (2) the structure is moderately to well preserved with clearly discernible complex crater morphologic features; (3) the crater is well exposed and covered by minimal to sparse vegetation; and (4) the structure has been well characterized, sampled and geologically mapped, and also offers reasonable access to the undisturbed target sequence stratigraphy for comparison with mapping both in the field and via remote sensing. Such factors are important to note here, as they are particularly relevant to remote-sensing studies of impact structures elsewhere on Earth.

Although the primary objective of this study was a proof of concept for spectral mapping of impact-exposed mineral and lithological compositions on Mars, this study highlights various aspects of terrestrial complex craters that are complementary to the second case study of a simple crater and, therefore, are relevant to this chapter. For a complete summary of the history and geology of Haughton, see Chapter 19.

13.8.1.1 *Spectral and lithological characterization*

A spectral unit map of the Haughton structure was created using standard image contrast stretches, band ratios and both MNF and PC algorithms on the ETM+ and ASTER scenes (Tornabene *et al.*, 2005). Maps generated using the 30 m/pixel Landsat Enhanced Thematic Mapper+ (ETM+) and ASTER SWIR data (Fig. 13.4) were very useful, as the VNIR wavelengths covered by these instruments are particularly sensitive to the carbonates and

hydrated sulfates that make up a major portion of Haughton's pre-impact target sequence (Osinski *et al.*, 2005). Spectral units (i.e. units of contiguous spectral similarity) defined using SWIR and TIR datasets were lithologically characterized in a similar fashion to the case study presented on Meteor Crater (Section 13.8.2). TIR-derived IEM spectra were matched to rock and mineral spectra from a library compiled and described by Christensen *et al.* (2000). These results were then ground-truthed with laboratory-collected spectra of samples obtained in the field, and via a direct comparison of our spectral/lithological maps with the lithostratigraphic map constructed from previous workers (Thorsteinsson and Mayr, 1987; Osinski *et al.*, 2005).

13.8.1.2 *Results and discussion*

An understanding of fresh complex crater structure and morphology observed on other planetary surfaces enables recognition of similar features at Haughton. Despite the estimated approximately 200 m of erosion at the HIS (Grieve, 1988; Osinski *et al.*, 2005), it is well preserved compared with many complex impact structures on Earth. The preservation and morphology of the HIS are readily observed in a colourized DTM of the structure (Fig. 13.4a). Elevation profiles derived from the DTM compare favourably to an ideal cross-section of a complex crater despite the level of degradation, infilling and other post-impact modification of the structure (see Chapter 19). The most readily recognizable feature in the colourized DTM is the presence of a circular depression bounded by a zone of circumferential listric faults. The concentric faults are indicative of a complex crater's rim and wall-terrace region (Fig. 13.4a), which is formed during the modification stage of complex crater formation (Chapter 5). On the northeast side of the structure, we can observe that one of these arcuate listric faults has been clearly exploited by ongoing fluvial erosion. Raised topography in the central region is consistent with a structural uplift, typical of complex craters; however, this interpretation cannot be based on topography/morphology alone. In addition, it is important to note that wall terraces can form in volcanic craters/calderas, so their presence is not necessarily diagnostic of an impact origin either. However, by linking these features observed in the DTM and in the visible images along with the spectral/lithological units from complementary spectral datasets (below), the relationships between the observed lithologies and morphologic expression of the structure, especially where compared with the lithological succession observed in the undisturbed target sequence, provides the best evidence for an impact (i.e. exogenic) origin versus an endogenic one (e.g. calderas, sinkholes, glacial features, salt domes). Unfortunately, erosion at the HIS has left no evidence of an ejecta blanket, which, if present, can be recognized in DTMs (e.g. Fig. 13.3e and Fig. 13.4a) and aerial/satellite imagery of other impact structures.

Combing our spectral results with the digital elevation from the DTM provides an important synthesis that allows the HIS to be recognized as a complex crater and the pre-impact target stratigraphy to be deciphered and reconstructed. In the case of stratified targets, complex craters preserve the relative succession and increasing depth of stratigraphic units in the pre-impact target within their features (e.g. wall terraces, central uplift).

These subsurface materials are exposed at the surface from a depth that is directly scaled to the size of the crater (Housen *et al.*, 1983; Schmidt and Housen, 1987; Melosh, 1989). These estimates provide a means to approximate quantitative depths of excavation and uplift of the lithologies exposed. Complex craters are of particular interest for reconstructing subsurface and shallow crustal stratigraphy, because they excavate rocks and minerals from both the immediate subsurface (e.g. within crater walls, terraces and ejecta) and from the shallow crust via stratigraphic uplift in a central feature (see Chapter 5).

All of the major units sampled and exposed by the Haughton impact event can be identified and mapped by remote-sensing techniques alone. The gentle regional tilt (~3–5° to the WSW) of the stratigraphy in the vicinity of Haughton conveniently offers the means to compare the lithologies exposed by the crater with the undisturbed target sequence just to the west of the crater (Fig. 13.4) – both from orbit and in the field. The matched compositions summarized below correlate and agree with the lithological units and the pre-impact stratigraphic sequence as mapped during recent field studies of the HIS (Chapter 19; Tornabene *et al.*, 2005). Units undisturbed by the HIS and the position of their equivalents exposed by the HIS are consistent with a complex crater and an impact origin. The summarized progression from the shallowest subsurface unit exposed within the rim to the deepest exposed unit within the central uplift reveals: dolomitic limestone in the 'rim area' and wall terraces; limestone in the wall/ terraces; gypsum-rich carbonate (eastern floor exposure); and limestone in the central uplift.

Dolomitic limestone occurs in the eroded crater 'rim area' (i.e. the elevated circumferential peaks surrounding the HIS) and represents the shallowest unit in the target sequence exposed by the HIS. Alternating dolomite and limestone outcrops that repeat on the eastern side of the crater are the clearest example of a set of terraces exposing the uppermost units of the pre-impact target sequence (Fig. 13.3c,d). The presence of two, or possibly three, crater terraces can be observed as a repetition of these two units, which correlates with the zone of concentric faults observed in the profiles derived from the HIS DTM. Together, these two lithological units, including the dolomitic limestone in the 'rim area', are consistent with the dolomites and limestones of the Middle and Lower Members of the Allen Bay Formation and Thumb Mountain Formation (Osinski *et al.*, 2005). The rim and wall-terrace units are stratigraphically followed by gypsum-rich unit (Fig. 13.4) observed exposed on or near the 'crater floor', which correlates with the gypsum-rich portions of the Thumb Mountain Formation (Osinski *et al.*, 2005). These occurrences of Thumb Mountain Formation appear to be part of the lower portions of the wall terraces in the eastern portion of the HIS, but rather may represent shallow portions of the structural uplift exposed from the erosion of the structure. Limestone occurs again associated with small distinctive topographic peaks in the central region of the crater, interpreted to be limestones of the Eleanor River Formation (Osinski *et al.*, 2005; Tornabene *et al.*, 2005; Chapter 19) that were stratigraphically uplifted from approximately 1.1 to 1.5 km beneath the pre-impact surface (Osinski *et al.*, 2005). Uplifted blocks of limestone from the Eleanor River Formation are embayed by a crater moat unit (Fig. 13.4, Fig. 13.7), which was interpreted to be a mix of all major lithotypes and is

consistent with clast-rich impact melt rocks at Haughton (Osinski *et al.*, 2005; Tornabene *et al.*, 2005).

13.8.2   High-resolution airborne TIR of Meteor Crater, Arizona

Meteor Crater (also known as Barringer Crater) is located 69 km east of Flagstaff, Arizona, near the city of Winslow, Arizona. It is arguably the most well known impact crater in the world, despite the initial misinterpretation as being volcanic in origin due to its slightly squarish shape and proximity to the cinder cones and maar craters of the San Francisco volcanic field to the west (Gilbert, 1896). Furthermore, the lack of large buried iron mass below the crater, which was the prevailing assumption at the time for meteorite impacts, further perpetuated the belief of a volcanic origin for many decades (Barringer, 1905). One of the first scientific investigations of the crater was in 1891 by G.K. Gilbert, who concluded that the crater was hydrovolcanic in origin based on the shape and lack of erupted lava. It was not until the early 1960s, when the dynamics of hypervelocity impact crater formation were better understood and high-pressure silica (stishovite) was discovered, that the impact origins of the crater were confirmed (Shoemaker, 1960). Since Shoemaker's early pioneering work at Meteor Crater, numerous studies have examined the geology (Shoemaker and Kieffer, 1974; Roddy, 1978), post-crater formation weathering/erosion (Pilon *et al.*, 1991; Grant and Schultz, 1993), as well as the current surface conditions derived from remote sensing (Ramsey, 2002; Wright and Ramsey, 2006) (see Chapter 18 for further details on Meteor Crater).

The crater has provided an ideal test locale for numerous studies, particularly in the TIR region, because of its well-preserved state, semi-arid environment, paucity of vegetation, lithological exposures and low relief. The crater has been the target of ground-based, airborne and satellite-based TIR data collections, with the primary focus on the exposed crater ejecta and the aeolian reworking of those sediments into the distinctive northeast-trending wind-streak. The analysis of the aeolian processes using remote sensing was either focused on trying to confirm the amount of erosion that had taken place, and thus the palaeoclimatic conditions (Ramsey, 2002), or using the data as an analogue for similar studies on Mars (Wright and Ramsey, 2006). Because the amount and style of erosion of a crater's ejecta have a direct bearing on the past climatic and geological history, the possibility of further constraining these rates with remote sensing becomes important for exploration of different craters on Earth or other planetary bodies.

13.8.2.1   *Geology and crater formation*

Meteor Crater is located in north-central Arizona east of Canyon Diablo (Fig. 13.2a–c). The current age estimate places the crater at approximately 50 ka (Nishiizumi *et al.*, 1991), making it one of the most recent and well-preserved impact sites on Earth (Chapter 18). The impact of the iron meteorite produced a simple crater that is approximately 180 m deep and 1200 m in diameter with a 30–60 m high rim. The region contains NW-trending normal faults and orthogonal joint sets that are responsible for the unusual squarish appearance of the crater (Shoemaker and
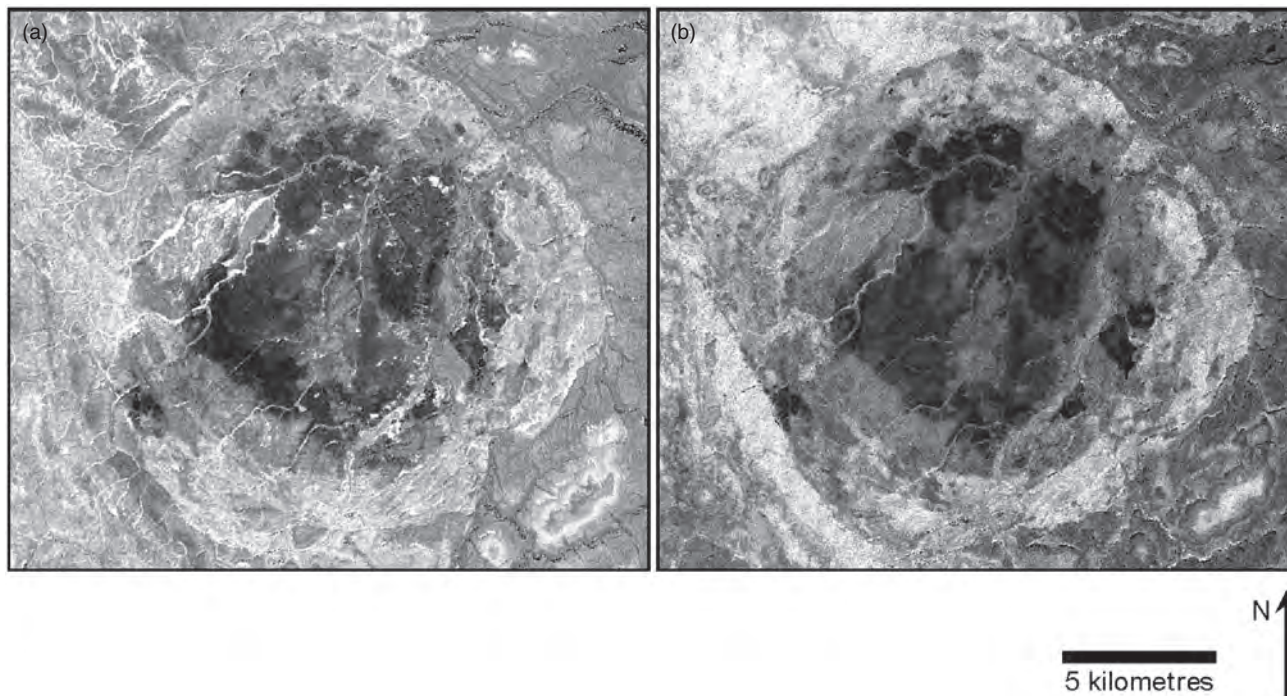
Figure 13.7 *Landsat 7* ETM+ band ratio images of the Haughton impact structure. (a) Band ratio image consisting of bands 5/7 (1.65 μm data divided by 2.215 μm data) highlights areas within the scene that may contain carbonates, phyllosilicates and various hydrothermal alteration minerals, which typically have absorption features in the VNIR in the vicinity of approximately 2.1–2.3 μm (band 7) and generally higher reflectance in the vicinity of 1.65 μm (band 5). In the case of Haughton, discrete high ratio-value areas on the eastern part of the crater floor correlate with gypsum of the Bay Fiord Formation and clays within the Haughton Formation in the vicinity of the Haughton River on the western end of the structure. Some sensitivity to carbonates is also exhibited in this band ratio combination. (b) Ratio of bands 3/2 (0.660 μm/0.560 μm) highlights areas bearing minerals rich (white) or poor (dark) in ferric iron. Fe^{2+} substitution for Mg^{2+} in the dolomites of the Allen Bay Formation is particularly prevalent in this image, whereas limestones and the impact melt-bearing breccias are particularly Fe^{2+} poor. The Fe^{2+}-poor nature of the crater floor 'melt' sheet may be a consequence of pervasive hydrothermal alteration (e.g. oxidation) of any Fe^{2+}-bearing materials that may have been incorporated into these deposits during and just shortly after impact (LandSat 7/NASA).

Kieffer, 1974). The principal flat-lying stratigraphic units (Permian Coconino Sandstone, Permian Kaibab Limestone and Triassic Moenkopi Formation) are preserved in inverted order as primary ejecta up to two crater radii (~1.2 km) away from the rim. These hummocky, near-rim ejecta deposits consist of a continuous blanket formed by larger blocks ranging in size from 0.5–30 m. The western, northern and eastern sides of the crater are dominated by Kaibab Formation ejecta with several lobate deposits of Coconino Sandstone interspersed. On the southern rim, the vast majority of the deposit consists of Coconino Sandstone, which is easily discernible due to its high albedo. Because of its friability and high porosity, this deposit has been the source for the majority of material that now comprises the northeast-trending patchy wind-streak (Fig. 13.8). To the west and south-west, the character of the hummocky ejecta is considerably more muted than the rest of the crater rim, likely due to mantling by aeolian fines transported by the dominant winds from the south-west. Within the crater, the uppermost floor deposits are formed from trapped airborne dust and basaltic ash from the nearby volcanic field. Below these surficial deposits, drill cores reveal 30 m of interfingered Quaternary lake beds and alluvium

overlying approximately 10 m of mixed impact breccia (Shoemaker and Kieffer, 1974).

13.8.2.2   Previous research results

On the basis of the apparent lack of mapped ejecta from units such as the Coconino Sandstone, previous studies by Shoemaker (1960) and Roddy (1978) reported 20–30 m of vertical erosion had occurred in the near-rim vicinity (~600 m). However, subsequent investigations concentrated on the distal ejecta field using ground-penetrating radar (Pilon *et al.*, 1991) and trenching/sieve analysis (Grant and Schultz, 1991) and found the total erosion was significantly lower (1–2 m). Based on these results, Grant and Schultz (1993) reinforced their argument of low erosion by citing the apparent lack of any appreciable amount of reworked Coconino Sandstone in the surrounding depositional traps. It was hypothesized that detectable volumes of reworked Coconino Sandstone should be present in these traps if the crater rim had been eroded by more than 20 m, unless this eroded material had been entirely removed from the region. Extensive transport and removal was not deemed likely based on the palaeoclimate
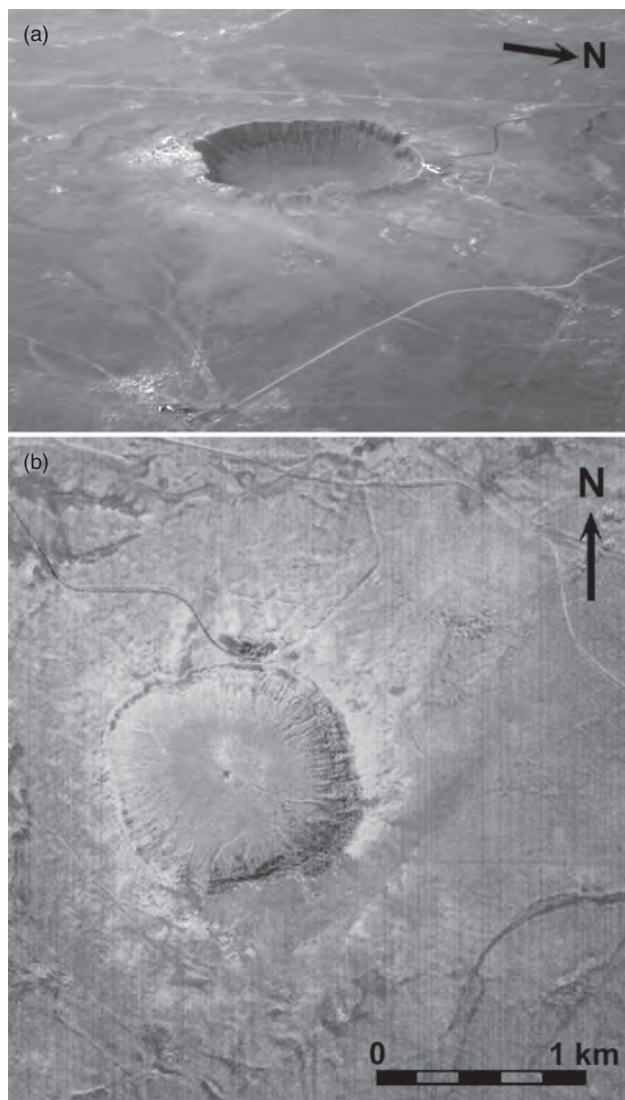
Figure 13.8   (a) Meteor Crater as seen from the east. (b) TIMS image with Coconino Sandstone spectral end-member displayed as red, Kaibab Limestone spectral end-member displayed as green and Moenkopi Formation (siltstone/mudstone in this region) displayed as blue. (see Colour Plate 32)

conditions in the region since the crater was formed, which suggest 1–2 cm of erosion per 1000 years (Greeley and Iverson, 1985) and is consistent with the lower estimate.

Several remote-sensing-based studies took place during the 1980s and 1990s at Meteor Crater. Garvin *et al.* (1989) examined airborne laser altimetry and characterized the nature and morphology of the near-rim hummocky ejecta. They found the ejecta was considerably less pronounced to the west and southwest and attributed it to aeolian burial by fines transported from the southwest. Later studies used TIR data to characterize the processes that produced the lithological composition of the ejecta deposits and wind streak.

Ramsey (2002) sought to validate the degree of erosion at Meteor Crater through the application of airborne TIR remote sensing. This study also served as an applied test of the linear deconvolution approach previously developed for unmixing laboratory-collected spectral mixtures data (Ramsey and Christensen, 1998). The results were also used to simulate data from Mars orbit to be acquired from the THEMIS instrument (Christensen *et al.*, 2003), similar to the other case study herein. Thermal Infrared Multispectral Scanner (TIMS) airborne data were acquired in 1994 at several different altitudes, which resulted in spatial resolutions from 3.2 to 10.9 m/pixel. The TIMS instrument had six spectral bands from 8 to 12 μm and was flown by NASA from 1982 to 1996 (Palluconi and Meeks, 1985). The highest spatial resolution data were used to extract spectral end-members from regions high in the three primary statigraphic units. The location of each of the end-member pixels was based on *a priori* knowledge of rock outcrops from field mapping and the strength of the spectral features observed in the processed emissivity data. The spectral end-members used with the linear deconvolution model produced images showing the relative spectral concentration of each IEM representative of the three lithologies (Fig. 13.8). These were compared with geological maps of the crater region (Shoemaker, 1960).

The TIMS intermediate flight line was chosen because it had good areal coverage as well as moderate spatial resolution to determine the areal extent and maximum traceable distance of the Coconino Sandstone. The Coconino comprised the uppermost layer of the wind-streak and was remotely detected up to five crater radii (3 km) to the northeast, with strong (>30%) concentrations as far out as 1 km. This is more extensive than the previously reported 0.5 crater radii from the crater rim (Grant and Schultz, 1993). Ramsey (2002) postulated that the reworked ejecta comprising the wind-streak is not strongly concentrated and consists of grains less than 300 μm, making it indistinguishable from the sediments derived from the other units and, therefore, easily overlooked in the field. In order to extend these lithological end-member maps from areal extent to eroded volume, an estimate of the sandstone ejecta thickness was made with the knowledge of the pixel size and an assumption of the volume of Coconino ejected based on theoretical modelling. This type of calculation is only accurate for the uppermost tens of micrometres because emitted TIR energy can only be detected to that depth. However, in conjunction with other geophysical data sets, it was extended to greater depths. Only pixels directly comprising the primary ejecta and wind-streak were counted. This end-member percentage summation was multiplied by the pixel resolution to produce the total areal coverage. Using this value and the theoretical maximum excavated volume proposed by Roddy (1978), an average thickness of 1.47 m was calculated. This estimate is consistent with the field and theoretical data and agrees with the values of Grant and Schultz (1993), but is far less than the original 20–30 m amount of Shoemaker (1960). It was the conclusion of this study that the lack of Coconino ejecta in the region surrounding Meteor Crater was caused by the differential uplift and subsequent ejection of the sedimentary units rather than a large amount of erosion post-impact.

Wright and Ramsey (2006) expanded upon the previous work by examining newly-acquired ASTER TIR data of the crater. ASTER was the Earth's first spaceborne multispectral TIR instrument to obtain high spatial resolution data. It has five bands in

the TIR region from 8.125 to 11.65 μm at 90 m/pixel spatial resolution. Unlike the previous study, end-members were statistically chosen in order to identify the most spectrally distinct pixel clusters in the ASTER emissivity data. These pixels were selected as IEMs, thereby requiring no prior knowledge of the surface geology. However, the lower spatial resolution of ASTER compared with that of TIMS produced clear spectral mixing of the IEMs. Wright and Ramsey (2006) found that the areal abundances derived from the deconvolution of the ASTER data were within 6% of those derived from the higher spatial and spectral resolution TIMS data. Furthermore, the areal extent of the wind-streak was found to be 2.7 km from the crater rim compared with 2.4 km calculated by Ramsey (2002). Therefore, it was determined that, despite a resolution degradation of nearly 800% from the TIMS data, the ASTER data produced similar results. This indicated the spatial scale of lithological mixing in the TIR pixels likely became homogeneous at scales larger than approximately 10–15 m and, therefore, validated the use of TIR data on the order of 100 m/pixel for similar studies of Earth and Mars.

13.8.2.3   Applicability to other craters

For craters that are significantly older and more modified/mantled, TIR remote sensing can also be used to determine other surface parameters. Roter Kamm Crater, Namibia (Fig. 13.2), is dated to about 3.5 Ma, is approximately 2.5 km in diameter and is located in the arid Namib Desert. It has been well mantled by active, broad sand dunes emanating from a larger sand sheet to the north (Fig. 13.2e). The target includes primarily Precambrian crystalline rocks and outcrops of impact melt breccias are found exclusively on the crater rim (Grant, 1999). Compositional analysis of the TIR data indicates that the region is dominated by two slightly different compositions of sand, which completely mantle the crater, the rim and the ejecta. However, the thermophysical properties of mantled surfaces become more obvious if the ATI image is examined. For Earth, we have a limited understanding of the relationships between the thermophysical data and natural surfaces. Thermal inertia can be approximated using the ATI, which is a comparison of the day/night temperature difference to the complement of one minus the daytime VNIR–SWIR-derived albedo. The ATI image of Roter Kamm Crater shows the crater rim and regions to the southwest to have higher values (Fig. 13.2g,h). These locations also agree well with spaceborne radar data of the region, which show radar-rough surfaces in the same locations. These higher ATI values are approximately half of those extracted from rock outcrops in the mountains 10 km to the east, indicating that even these surfaces are likely mantled to some degree. ATI data can give a good indication of the degree of mantling and presence of blocky ejecta and the crater rim rocks up to several metres below the exposed surface (Putzig and Mellon, 2007).

13.9   Concluding remarks

The above case studies demonstrate the use of airborne and orbital data to provide compositional details for preserved, well-exposed and non-vegetated structures and how craters can be used as a means to map subsurface lithologies for constraints on stratigraphy. By using ASTER and ETM+ datasets as analogues for Mars remote-sensing instruments, the study of the Haughton structure serves as a terrestrial proof of concept that subsurface geology of Mars may be successfully mapped via moderately to well-preserved impact craters that are not obscured by dust or other surface deposits. Had it not been for the regional tilt of the stratigraphic target sequence, the HIS would be completely surrounded by the dolomite with the only subsurface exposures of lower stratigraphic units occurring within nearby valleys and within the excavated and uplifted target materials outcropping within the impact structure as a natural 'window' into the crust (Tornabene *et al.*, 2005). Because tectonic processes are less pervasive on Mars and other terrestrial bodies than on Earth, impact craters provide the most convenient means to locate, map and identify the diverse mineral and lithological compositions within planetary crusts.

For younger craters where the primary ejecta is still present, remote sensing provides an ideal way to characterize the amount of erosion, the distribution and its thickness. At Meteor Crater, these parameters were constrained using TIR remote sensing. This work not only demonstrated the utility of using remote sensing for insight into the crater formation and subsequent erosional processes, but also the geological history of a region. Using the unique spectral characteristics of a lithology not otherwise observable at the surface if not for impact, the areal extent and volume of that ejected lithology were calculated. Comparable investigations of the surfaces of other planets and moons are warranted where only remote data exist.

Whether searching for new impact sites or through detailed analyses of known impact structures, remote sensing provides an approach to extract quantitative aspects or details that would not otherwise be known from the field. This ranges from identifying terrestrial impact structures via morphology and topography to analyses of the composition or physical properties of the materials affected by impact. This chapter represents a summary of what properties can be determined from the analyses of remote sensing.

References

Adams, J.B., Smith, M.O. and Gillespie, A.R. (1993) Imaging spectroscopy: interpretation based on spectral mixture analysis, in *Remote Geochemical Analysis: Elemental and Mineralogical Composition* (eds C.M. Pieters and P.A. Englert), Cambridge University Press, New York, NY, 145–166.

ASTER (2010) ASTER global digital elevation model, http://www.ersdac.or.jp/GDEM/E/4.html.

Bandfield, J., Ghent, R., Vasavada, A. *et al.* (2011) Lunar surface rock abundance and regolith fines temperatures derived from LRO Diviner Radiometer data. *Journal of Geophysical Research*, 116, E00H02. DOI: 10.1029/2011JE003866.

Barlow, B.C. (1979) Gravity investigations of the Gosses Bluff impact structure, central Australia. *Journal of Australian Geology and Geophysics*, 4, 323–329.

Barringer, D.M. (1905) Coon Mountain and its crater. *Proceedings of the Academy of Natural Sciences of Philadelphia*, 66, 861–886.

Boardman J.W. and Kruse F.A. (1994) Automated spectral analysis: a geological example using AVIRIS data, north Grapevine Mountains, Nevada. Proceedings, ERIM 10th Thematic Conference on Geologic Remote Sensing, pp. I-407–I-418.

Boynton, W.V., Feldman, W.C., Mitrofanov, I.G. *et al.*, (2004) The Mars Odyssey Gamma-Ray Spectrometer instrument suite. *Space Science Reviews*, 110, 37–83. DOI: 10.1023/B:SPAC.0000021007.76126.15.

Brown, R.H., and 21 colleagues, (2004) The *Cassini* Visual and Infrared Mapping Spectrometer (VIMS) investigation. *Space Science Reviews*, 115, 111–168. DOI: 10.1007/s11214-004-1453-x.

Bufton, J.L., Garvin, J.B., Cavanaugh, J.F. *et al.* (1991) Airborne lidar for profiling of surface topography. *Optical Engineering*, 30, 72–78.

Campbell, D.B., Stacy, N.J.S., Newman, W.I. *et al.* (1992) Magellan observations of extended impact crater related features on the surface of Venus. *Journal of Geophysical Research*, 97, 16249–16278.

Carter, A.J., Ramsey, M.S., Durant, A.J. *et al.* (2009) Micron-scale roughness of volcanic surfaces from thermal infrared spectroscopy and scanning electron microscopy. *Journal of Geophysical Research*, 114, B02213. DOI: 10.1029/2008JB005632.

Chadwick, D.J. and Schaber, G.G. (1993) Impact crater outflows on Venus: morphology and emplacement mechanisms. *Journal of Geophysical Research*, 98 (E11), 20891–20902.

Christensen, P.R., Bandfield, J.L., Hamilton, V.E. *et al.* (2000) A thermal emission spectral library of rock forming minerals. *Journal of Geophysical Research*, 105, 9735–9739.

Christensen, P.R., Bandfield, J.L., Bell III, J.F. *et al.* (2003) Morphology and composition of the surface of Mars: *Mars Odyssey* THEMIS results. *Science*, 300, 2056–2061.

Cracknell, A.P. and Xue, Y. (1996) Thermal inertia determination from space – a tutorial review. *International Journal of Remote Sensing*, 17 (3), 431–461. DOI: 10.1080/01431169608949020.

D'Aria, D. and Garvin, J.B. (1988) Thermal infrared reflectance spectroscopy of impact-related rocks: implications for geologic remote sensing of Mars and Earth. Lunar and Planetary Science Conference XIX, pp. 243–244

Farr, T.G., Rosen, P.A., Caro, E. *et al.* (2007) The Shuttle Radar Topography Mission. *Reviews of Geophysics*, 45, RG2004. DOI: 10.1029/2005RG000183.

Fergason, R.L., Christensen, P.R. and Kieffer, H.H. (2006) High resolution thermal inertia derived from THEMIS: thermal model and applications. *Journal of Geophysical Research*, 111, E12004. DOI: 12010.11029/12006JE002735.

Folco, L., Di Martino, M., El Barkooky, A. *et al.* (2010) The Kamil Crater in Egypt. *Science*, 329, 804. DOI: 10.1126/science.1190990.

Folco, L., Di Martino, M., El Barkooky, A. *et al.* (2011) Kamil Crater (Egypt): ground truth for small-scale meteorite impacts on Earth. *Geology*, 39, 179–182. DOI: 10.1130/G31624.1

French, B.M. (1998) *Traces of Catastrophe: A Handbook of Shock-Metamorphic Effects in Terrestrial Impact Structures*, LPI Contribution No. 954, Lunar and Planetary Institute, Houston, TX.

Garvin, J.B., Bufton, J.L., Campell, B.A. and Zisk, S.H. (1989) Terrain analysis of Meteor Crater ejecta blanket. Lunar and Planetary Science Conference XX, pp. 333–334.

Garvin, J.B., Schnetzler, C.C. and Grieve, R.F. (1992) Characteristics of large terrestrial impact structures as revealed by remote sensing studies. *Tectonophysics*, 216, 45–62.

Gilbert, G.K. (1896) The origin of hypotheses, illustrated by the discussion of a topographical problem. *Science*, 3, 1–13.

Gillespie, A.R. (1992) Spectral mixture analysis of multispectral thermal infrared images. *Remote Sensing of Environment*, 42, 137–145.

Gillespie A.R., Kahle A.B. and Walker, R.E. (1986) Color enhancement of highly correlated images. 1. Decorrelation and HSI contrast stretches. *Remote Sensing of Environment*, 20, 209–235.

Gillespie, A.R., Matsunaga, T., Rokugawa, S. and Hook, S.J. (1998) Temperature and emissivity separation from Advanced Spaceborne Thermal Emission and Reflection Radiometer (ASTER) images. *IEEE Transactions on Geoscience Remote Sensing*, 36, 1113–1126.

Grant J.A. (1999) Evaluating the evolution of process specific degradation signatures around impact craters. *International Journal of Impact Engineering*, 23, 331–340.

Grant, J.A. and Schultz, P.H. (1991) Characteristics of ejecta and alluvial deposits at Meteor Crater, Arizona and Odessa Craters, Texas: results from ground penetrating radar. Lunar and Planetary Science Conference XXII, pp. 481–482.

Grant, J.A. and Schultz, P.H. (1993) Erosion of ejecta at Meteor Crater, Arizona. *Journal of Geophysical Research*, 98, 15033–15047.

Grant, J.A., Irwin, R.P., Grotzinger, J.P. *et al.* (2008) HiRISE imaging of impact megabreccia and sub-meter aqueous strata in Holden Crater, Mars. *Geology*, 36, 195–198.

Greeley, R. and Iverson, J.D. (1985) *Wind as a Geological Process on Earth, Mars, Venus, and Titan*, Cambridge University Press, New York, NY.

Grieve, R.A.F. (1988) The Haughton impact structure: summary and synthesis of the results of the HISS project. *Meteoritics*, 23, 249–254.

Hamilton, V.E. (2003) Thermal infrared emission spectroscopy of titanium-enriched pyroxenes. *Journal of Geophysical Research*, 108, 5095. DOI: 10.1029/2003JE002052.

Housen K.R., Schmidt R.M. and Holsapple K.A. (1983) Crater ejecta scaling laws – fundamental forms based on dimensional analysis. *Journal of Geophysical Research*, 88, 2485–2499.

Hudson Jr, R.D. (1969) *Infrared System Engineering*, John Wiley and Sons, Inc., New York, NY.

Hunt, G.R. (1980) Electromagnetic radiation: the communication link in remote sensing, in *Remote Sensing in Geology* (eds B.S. Siegel and A.R. Gillespie), John Wiley and Sons, Inc., New York, NY, pp. 5–45.

Jensen, J.R. (2007) *Remote Sensing of the Environment: An Earth Resource Perspective*, 2nd edn, Prentice Hall (ISBN: 0-13-188950-8).

Johnson, J.R., Hörz, F., Lucey, P.G. and Christensen, P.R. (2002) Thermal infrared spectroscopy of experimentally shocked anorthosite and pyroxenite: implications for remote sensing of Mars. *Journal of Geophysical Research*, 107 (E10), 5073. DOI: 10.1029/2001JE001517.

Johnson, J.R., Staid, M.I. and Kraft, M.D. (2007) Thermal infrared spectroscopy and modeling of experimentally shocked basalts. *American Mineralogist*, 92, 1148–1157.

Koeberl, C. (2004) Remote sensing studies of impact craters: how to be sure? *Comptes Rendus Geoscience*, 336, 959–961.

Le Mouélic, S., Paillou, P., Janssen, M.A. *et al.*, (2008) Mapping and interpretation of Sinlap crater on Titan using *Cassini* VIMS and RADAR data. *Journal of Geophysical Research*, 113, E04003. DOI: 10.1029/2007JE002965.

Lillesand, T.M. and Kiefer, R.W. (2000) *Remote Sensing and Image Interpretation*, John Wiley and Sons, Inc., New York, NY.

Lorenz, R.D., Wood, C.A., Lune, J.I. *et al.* (2007) Titan's young surface: initial impact crater survey by *Cassini* RADAR and model comparison. *Geophysical Research Letters*, 34, L07204. DOI: 10.1029/2006GL028971.

Lyon, R.J.P. (1965) Analysis of rocks by spectral infrared emission (8 to 25 microns). *Economic Geology*, 60, 715–736.
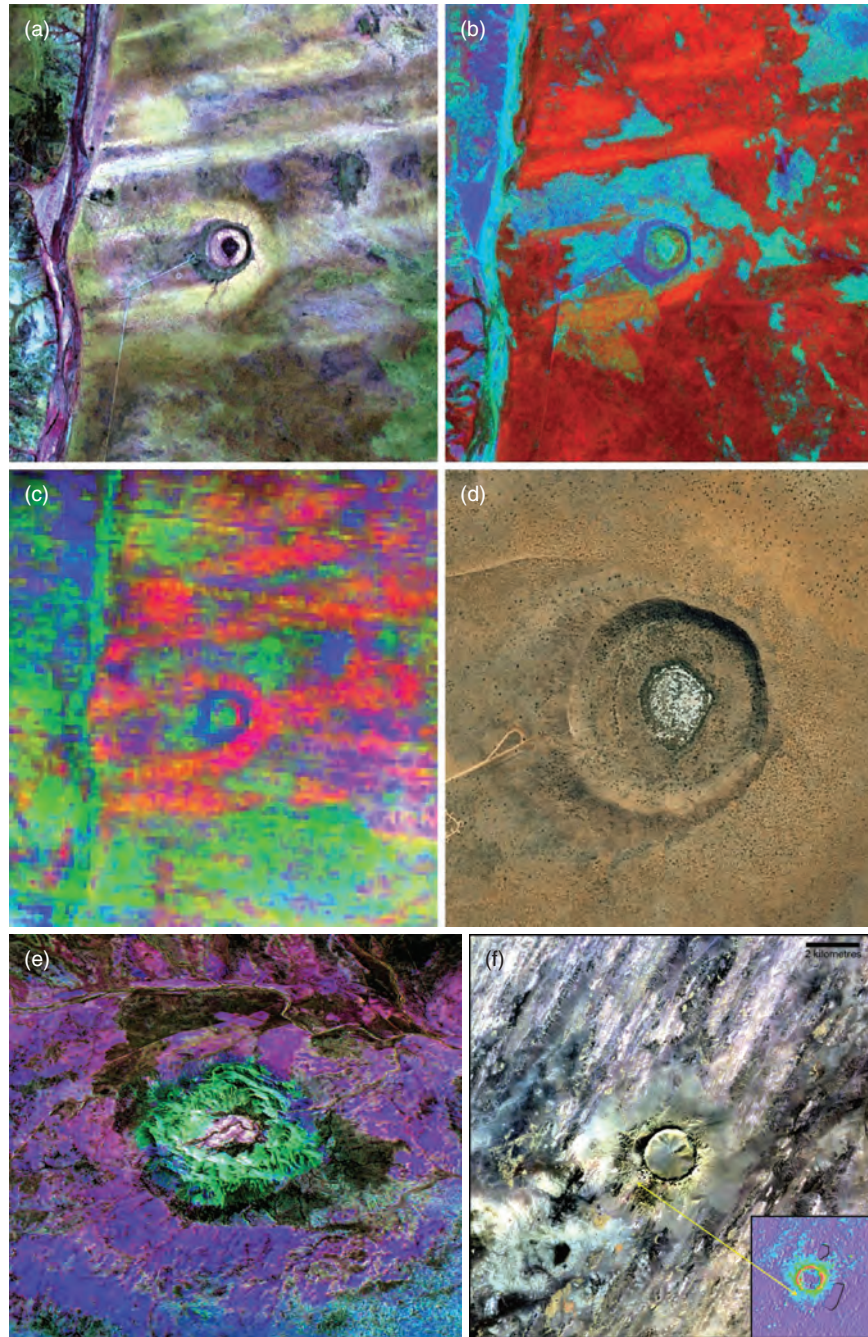
Marzo, G.A., Davila, A.F., Tornabene, L.L. *et al.* (2010) Evidence for Hesperian impact-induced hydrothermalism on Mars. *Icarus*, 208, 667–683. DOI: 10.1016/j.icarus.2010.03.013.

Masursky, H., Eliason, E., Ford, P.G. *et al.* (1980) Pioneer Venus radar results: geology from images and altimetry. *Journal of Geophysical Research*, 85 (A13), 8232–8260. DOI: 10.1029/JA085iA13p08232.

Melosh, H.J. (1989) *Impact Cratering: A Geologic Process*, Oxford University Press.

Nishiizumi, K., Kohl, C.P., Shoemaker, E.M. *et al.* (1991) *In situ* [10]Be–[26]Al exposure ages at Meteor Crater, Arizona. *Geochimica et Cosmochimica Acta*, 55, 2699–2703.

Nowicki, S.A. and Christensen, P.R. (2007) Rock abundance on Mars from the Thermal Emission Spectrometer. *Journal of Geophysical Research (Planets)*, 112, 5007. DOI: 10.1029/2006JE002798.

Osinski, G.R., Lee, P., Spray, J.G. *et al.* (2005) Geological overview and cratering model for the Haughton impact structure, Devon Island, Canadian High Arctic. *Meteoritics and Planetary Science*, 40, 1759–1776. DOI: 10.1111/j.1945-5100.2005.tb00145.x.

Palluconi, F.D. and Meeks, G.R. (1985) Thermal infrared multispectral scanner (TIMS): an investigators guide to TIMS data. JPL Publication 85-32, Jet Propulsion Laboratory, Pasadena, CA.

Pelkey, S.M., Jakosky, B.M. and Mellon, M.T. (2001) Thermal inertia of crater-related wind streaks on Mars. *Journal of Geophysical Research*, 106, 23909–23920.

Pettengill, G.H., Eliason, E., Ford, P.G. *et al.* (1980) Pioneer Venus radar results altimetry and surface properties. *Journal of Geophysical Research*, 85 (A13), 8261–8270. DOI: 10.1029/JA085iA13p08261.

Phillips, R.J., Arvidson, R.E., Boyce, J.M. *et al.* (1991) Impact craters on Venus: initial analysis from *Magellan*. *Science*, 252, 288–297. DOI: 10.1126/science.252.5003.288.

Pilon, J.A., Grieve, R.A.F. and Sharpton, V.L. (1991) The subsurface character of Meteor Crater, Arizona, as determined by ground-probing radar. *Journal of Geophysical Research*, 96, 15563–15576.

Prentice, C.S., Crosby, C.J., Whitehill, C.S. *et al.*, (2009) Illuminating northern California's active faults. *EOS, Transactions, American Geophysical Union*, 90 (7), 55–56.

Prinz, T. (1996) Multispectral remote sensing of the Gosses Bluff impact crater, central Australia (N.T.) by using Landsat-TM and ERS-1 data. *Journal of Photogrammetry and Remote Sensing*, 51, 137–149.

Putzig, N.E. and Mellon, M.T. (2007) Apparent thermal inertia and the surface heterogeneity of Mars. *Icarus*, 191, 68–94.

Ramsey, M.S. (2002) Ejecta distribution patterns at Meteor Crater, Arizona: on the applicability of lithologic end-member deconvolution for spaceborne thermal infrared data of Earth and Mars. *Journal of Geophysical Research*, 107, 5059. DOI: 10.1029/2001JE001827.

Ramsey, M.S. and Christensen, P.R. (1998) Mineral abundance determination: quantitative deconvolution of thermal emission spectra. *Journal of Geophysical Research*, 103, 577–596.

Ramsey, M.S. and Fink, J.H. (1999) Estimating silicic lava vesicularity with thermal remote sensing: a new technique for volcanic mapping and monitoring. *Bulletin of Volcanology*, 61, 32–39.

Realmuto, V. (1990) Separating the effects of temperature and emissivity: emissivity spectrum normalization, in *Proceedings of the Second Annual Airborne Earth Science Workshop*, vol. 2 (ed. E.A. Abbott), JPL Publication 90-55, Jet Propulsion Laboratory, Pasadena, CA, pp. 31–35.

Roddy, D.J. (1978) Pre-impact geologic conditions, physical properties, energy calculations, meteorite and initial crater dimensions and orientations of joints, faults and walls at Meteor Crater, Arizona. *Proceedings of the Lunar and Planetary Science Conference*, 9, 3891–3980.

Rowan L.C. and Mars J.C. (2003) Lithologic mapping in the Mountain Pass, California area using Advanced Spaceborne Thermal Emission and Reflection Radiometer (ASTER) data. *Remote Sensing of the Environment*, 84, 350–366.

Sabins, F.F. (1997) *Remote Sensing: Principles and Interpretation*, W.H. Freeman and Company, New York, NY.

Salisbury, J.W. (1993) Mid-infrared spectroscopy: laboratory data, in *Remote Geochemical Analysis: Elemental and Mineralogical Composition* (eds C.M. Pieters and P.A. Englert), Cambridge University Press, New York, NY, pp. 79–98.

Salisbury, J.W. and D'Aria, D.M. (1992) Emissivity of terrestrial materials in the 8–14 µm atmospheric window. *Remote Sensing of Environment*, 42, 83–106.

Salisbury, J.W. and Wald, A. (1992) The role of volume scattering in reducing spectral contrast of reststrahlen bands in spectra of powdered minerals. *Icarus*, 96, 121–128.

Salisbury, J.W. and Walter, L.S. (1989) Thermal infrared (2.5–13.5 µm) spectroscopic remote sensing of igneous rock types on particulate planetary surfaces. *Journal of Geophysical Research*, 94, 9192–9202.

Saunders, R.S., Pettengill, G.H., Arvidson, R.E. *et al.* (1990) The *Magellan* Venus radar mapping mission. *Journal of Geophysical Research*, 95 (B6), 8339–8355. DOI: 10.1029/JB095iB06p08339.

Schaber, G.G., Strom, G.H., Moore, H.J. *et al.* (1992) Geology and distribution of impact craters on Venus: what are they telling us? *Journal of Geophysical Research*, 97 (E8), 13257–13301.

Schmidt, R.M. and Housen, K.R. (1987) Some recent advances in the scaling of impact and explosion cratering. *International Journal of Impact Engineering*, 5, 543–560.

Shoemaker, E.M. (1960) Impact mechanics at Meteor Crater, Arizona. PhD dissertation, Princeton University.

Shoemaker, E.M. and Kieffer, S.W. (1974) *Guidebook to the Geology of Meteor Crater, Arizona*, Arizona State University Center for Meteorite Studies Publication 17, Center for Meteorite Studies, Arizona State University, Tempe, AZ.

Smith, D.E., Zuber, M.T., Frey, H.V. *et al.* (2001) Mars Orbiter Laser Altimeter: experiment summary after the first year of global mapping of Mars. *Journal of Geophysical Research*, 106, 23689–23722. DOI: 10.1029/2000JE001364.

Smith, D.E., Zuber, M.T., Neumann, G.A. *et al.* (2010) Initial observations from the Lunar Orbiter Laser Altimeter (LOLA). *Geophysical Research Letters*, 37, L18204. DOI: 10.1029/2010GL043751.

Stewart, S.T. and Valiant, G.J. (2006) Martian subsurface properties and crater formation process inferred from fresh impact crater geometries. *Meteoritics*, 41, 1509–1537. DOI: 10.1111/j.1945-5100.2006.tb00433.x.

Thomson, J.L. and Salisbury, J.W. (1993) The mid-infrared reflectance of mineral mixtures (7–14 µm). *Remote Sensing of Environment*, 45, 1–13.

Thorsteinsson R. and Mayr U. (1987) *The Sedimentary Rocks of Devon Island, Canadian Arctic Archipelago*, Geological Survey of Canada Memoir 411, Geological Survey of Canada, Ottawa.

Tornabene, L.T. Moersch, J.E., Osinski, G.R. *et al.* (2005) Spaceborne visible and thermal infrared lithologic mapping of impact-exposed subsurface lithologies at the Haughton impact structure, Devon Island, Canadian High Arctic: applications to Mars. *Meteoritics*, 40 (12), 1835–1858.

Van Zyl, J.J. (2001) The Shuttle Radar Topography Mission (SRTM): a breakthrough in remote sensing of topography. *Acta Astronautica*, 48, 559–565.

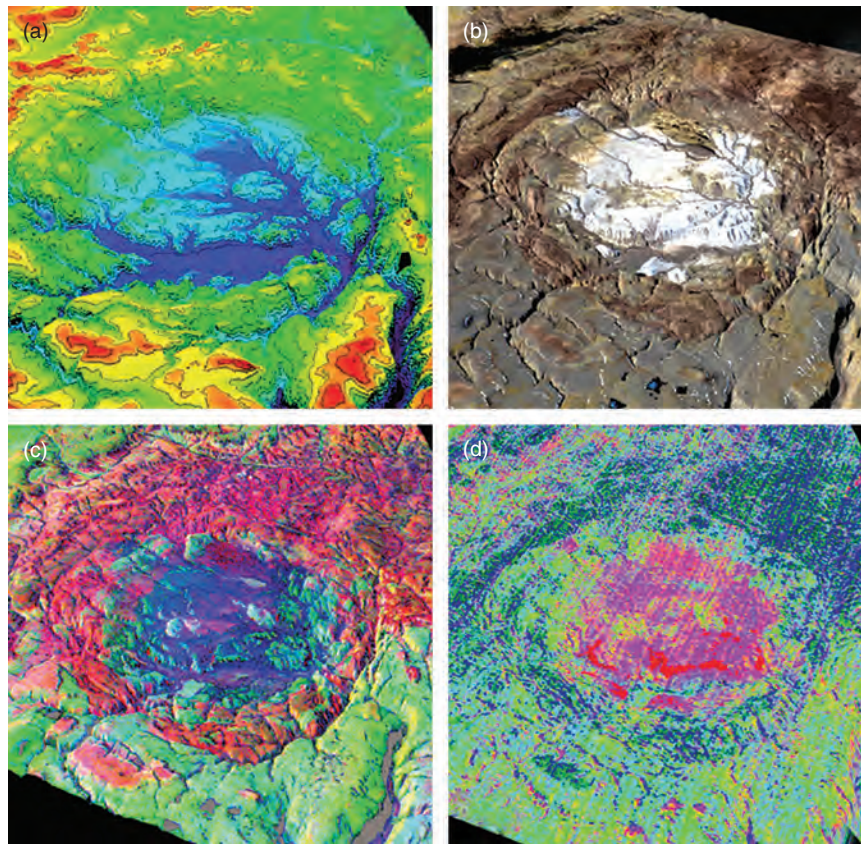Vincent, R.K. (1997) *Fundamentals of Geological and Environmental Remote Sensing*, Prentice Hall.

Webster, T.L., Murphy, J.B. and Gosse, J.C. (2006) Mapping subtle structures with light detection and ranging (LIDAR): flow units and phreatomagmatic rootless cones in the North Mountain Basalt, Nova Scotia. *Canadian Journal of Earth Sciences*, 43, 157–176.

Wood, C.A., Lorenz, R., Kirk, R. *et al.* (2010) Impact craters on Titan. *Icarus*, 206, 334–344. DOI: 10.1016/j.icarus.2009.08.021.

Woolard, J.W. and Colby, J.D. (2002) Spatial characterization, resolution, and volumetric change of coastal dunes using airborne LIDAR: Cape Hatteras, North Carolina. *Geomorphology*, 48, 269–287.

Wells, K.S., Campbell, D.B., Campbell, B.A. and Carter, L.M. (2010) Detection of small lunar secondary craters in circular polarization ratio radar images. *Journal of Geophysical Research*, 115, E06008. DOI: 10.1029/2009JE003491.

Wright, S.P. and Ramsey, M.S. (2006) Thermal infrared data analyses of Meteor Crater, Arizona: implications for Mars spaceborne data from the Thermal Emission Imaging System. *Journal of Geophysical Research*, 111, E02004. DOI: 10.1029/2005JE002472.

Wright, S.P., Christensen, P.R. and Sharp, T.G. (2011) Laboratory thermal emission spectroscopy of shocked basalt from Lonar Crater, India and implications for Mars orbital and sample data. *Journal of Geophysical Research*, 116, E09006. DOI: 10.1029/2010JE003785.

Zuber, M.T., Smith, D.E., Solomon, S.C. *et al.* (1992) The Mars Observer Laser Altimeter investigation. *Journal of Geophysical Research*, 97 (E5), 7781–7797. DOI: 10.1029/92JE00341.

Zumsprekel, H. and Bischoff, L. (2005) Remote sensing and GIS analyses of the Strangways impact structure, Northern Territory. *Australian Journal of Earth Science*, 52, 621–630.
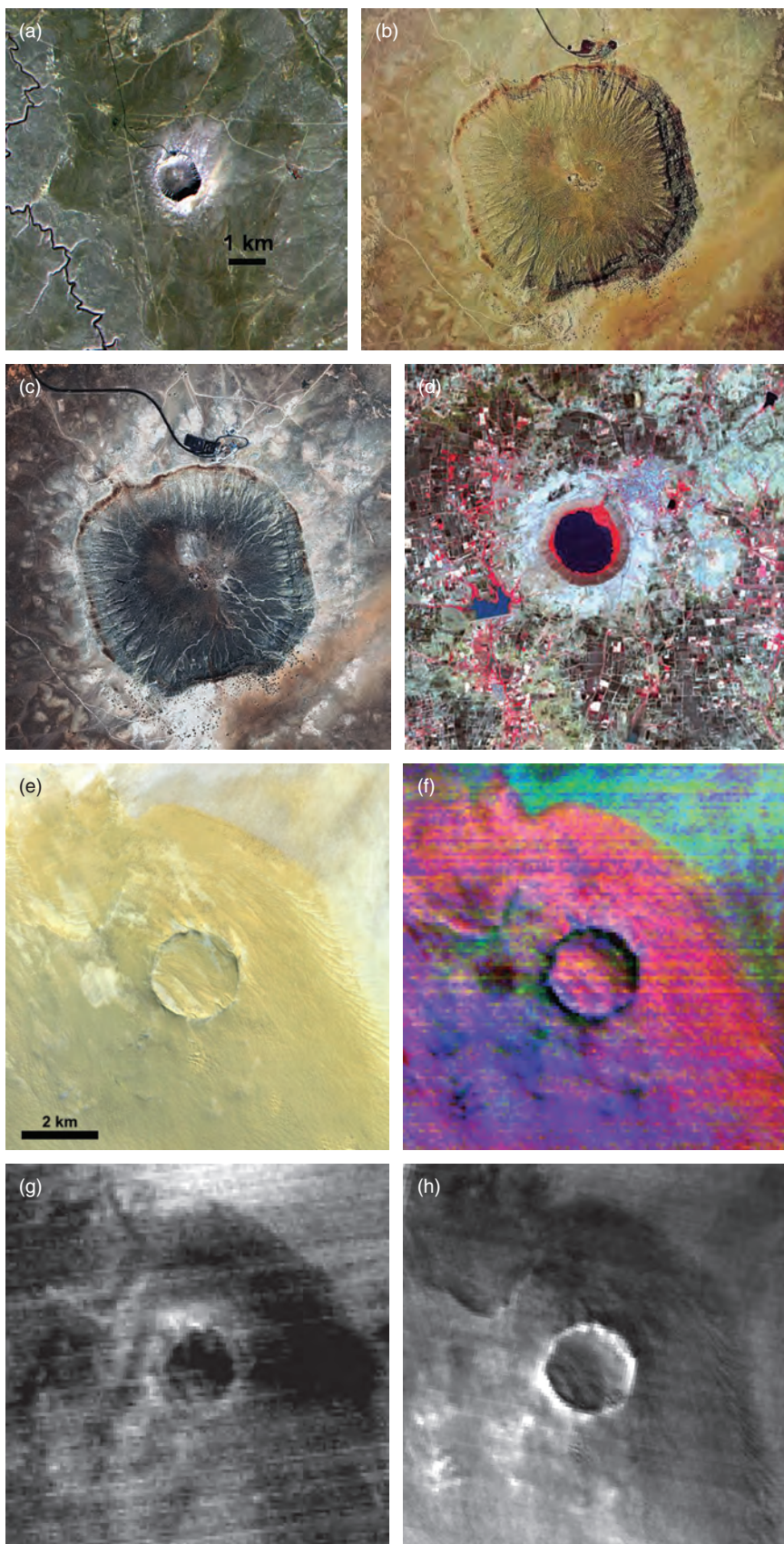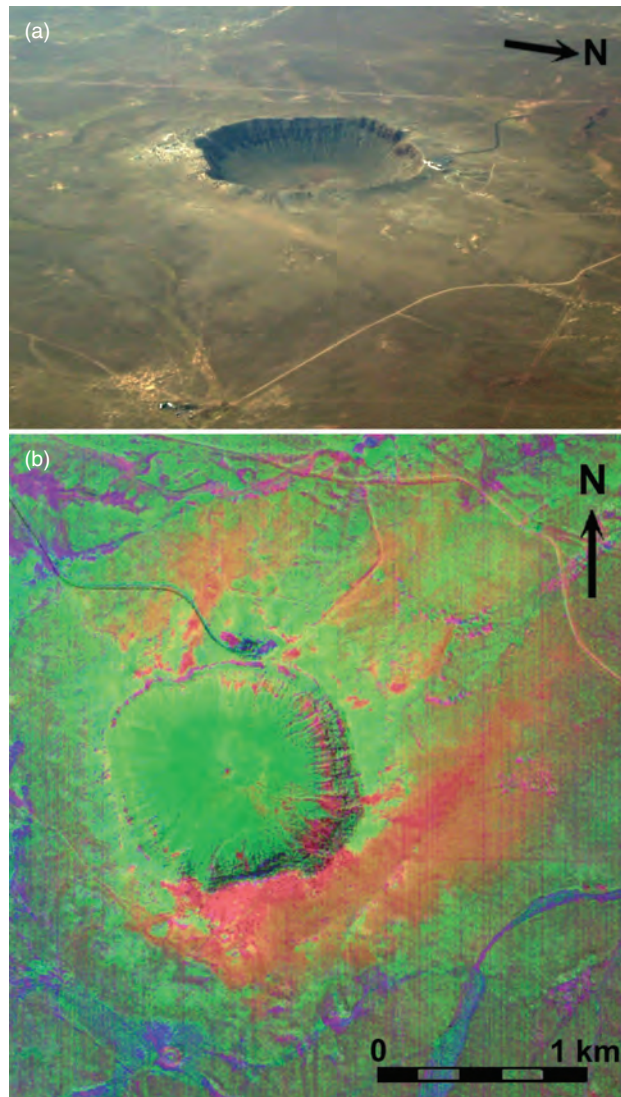
Plate 29 (Figure 13.2) (a) 15 m resolution ASTER VNIR of Meteor Crater, Arizona displayed as bands 3–2–1 in red–green–blue, showing very little vegetation save for a small farm with trees east of the crater. (b) True-colour aerial photograph of Meteor Crater with approximately 1 m resolution. (c) False-colour aerial photograph of Meteor Crater stretched to display ejecta lobes of bright-white Coconino and Kaibab ejecta. (d) False-colour ASTER VNIR image of Lonar Crater, India (Chapter 18), displayed as bands 3–2–1 in red–green–blue; vegetation (as red) can be seen circum the crater lake but inside the crater rim. (e)–(h) ASTER VNIR and TIR data of Roter Kamm, Namibia; (e) daytime VNIR colour image showing the pervasive mantling of aeolian sand; (f) daytime TIR decorrelation stretch of TIR bands 14, 12, 10 in R, G, B (respectively) indicating significant variability in the sand composition (Fe-rich silicate sands shown in blue/purple and non-Fe-rich silicates shown in red); (g) night-time temperature image showing less than 4 °C variation from crater rim to the near-rim ejecta; (h) apparent thermal inertia (ATI) image (see text) with high ATI values (bright) indicating potential blocky and less mantled ejecta. See text for explanations of acronyms.

Plate 30 (Figure 13.3)   Various remote images of the Wolfe Creek (a–d) and Gosses Bluff (e) craters in Australia. (a) ASTER VNIR image with bands 3, 2 and 1 displayed as red, green and blue, with a 2% stretch. Image taken 02-02-2003. (b) Landsat band ratio image with Fe ratio, normalized difference vegetation index and OH-bearing ratio (see text for details) displayed as red, green and blue. Data are stretched 2% to bring out differences. Image from 09-03-1999. (c) ASTER TIR decorrelation stretch with bands 14, 12 and 10 displayed as red, green and blue. Image from 02-02-2003. (d) High-resolution image derived from © Google Earth, 2012. (e) View to northwest of the 23 km diameter Gosses Bluff Crater, with a hue saturation value transformed VNIR with SWIR minimum noise fraction (MNF) bands applied to a VNIR image (15 m resolution) and draped on a DTM with a vertical exaggeration of 3. Green represents bedrock from several Mesozoic sandstone lithologies (Barlow, 1979; Prinz, 1996) uplifted above alluvium shown as blue and purple. (f) ASTER stereo-derived DEM and VNIR data covering the 1.9 km terrestrial impact structure Tenoumer located at 22°55′7″N, 10°24′29″W, in Mauritania, Africa. The 15 m/pixel colour infrared image of Tenoumer reveals what appears to be a two-facies, circumferential deposit around the crater rim reminiscent of ejecta around fresh impact craters on other planetary surfaces. The colour-coded DEM in the inset shows elevated terrain consistent with the inner most facies of these deposits, which strongly supports the idea that some ejecta was preserved around this infilled simple crater. The DEM shows similar to results from Meteor Crater (Garvin *et al.*, 1989), that the wind regime that has dominated this region since the time of crater formation has preferentially muted and eroded the windward (southwest) side. (Note: the two areas outlined in black and in solid purple are areas of spurious data values where difficulties due to surface or atmospheric properties confounded attempts to derive digital elevation for these areas.)

Plate 31 (Figure 13.4)   Morphometric and spectral maps (VNIR, SWIR and TIR) of the Haughton impact structure, Devon Island, Nunavut territory, Canada. North is to the bottom right of each subimage. (a) A 25 m colourized DTM of the Haughton impact structure (courtesy of the Natural Resources of Canada http://www.nrcan-rncan.gc.ca/com/index-eng.php), with the vertical exaggeration set to 10. (b) VNIR image from *Landsat 7* ETM+ (30 m/pixel). The impact melt rock of the Haughton Formation is the most apparent lithological unit. This is manifested as a white unit that predominately lines the crater floor, but smaller occurrences can also be observed in the vicinity of the wall/terraces and rim area. (c) ASTER SWIR (1.656–2.400 μm) colour composite of MNF-transformed bands using principle components 2, 1 and 6 in RGB (30 m/pixel). Lithological units are as follows: magenta, dolomite; cyan, limestone; red, gypsum; blue, impact melt rock. (d) ASTER TIR colour-composite using DCS bands 14, 12 and 10 (90 m/pixel; Tornabene *et al.*, 2005). Lithological units are as follows: dark blue–green is dolomite; cyan–light green is limestone; red is gypsum; and magenta–pink is impact melt rock.

Plate 32 (Figure 13.8) (a) Meteor Crater as seen from the east. (b) TIMS image with Coconino Sandstone spectral end-member displayed as red, Kaibab Limestone spectral end-member displayed as green and Moenkopi Formation (siltstone/mudstone in this region) displayed as blue.